EDMS Id: **1287413**

ORGANISATION EUROPEENNE POUR LA RECHERCHE NUCLEAIRE
EUROPEAN ORGANIZATION FOR NUCLEAR RESEARCH

Laboratoire Européen pour la Physique des Particules
European Laboratory for Particle Physics

HSE

Occupational Health & Safety and Environmental Protection

Technical Note

CERN-RP-2013-037-REPORTS-TN

Instrument intercomparison in the pulsed neutron fields at the CERN HiRadMat facility

E. Aza [a,b], M. Caresana [c], C. Cassell [c,d], N. Charitonidis [a,e], E. Harrouch [a], G.P. Manessi [a,f,], M. Pangallo [a], D. Perrin [a], E. Samara [a,g], M. Silari [a]

[a] CERN, CH-1211 Geneva 23, Switzerland
[b] Aristotle University of Thessaloniki, Department of Physics, GR-54124 Thessaloniki, Greece
[c] Politecnico of Milan, Department of Energy, Via Ponzio 34/3, IT-20133 Milan, Italy
[d] University of Wollongong, Centre for Medical Radiation Physics, NSW 2522
[e] École Polytechnique Fédérale de Lausanne, Particle Accelerator Physics Laboratory, CH-1015 Lausanne, Switzerland
[f] University of Liverpool, Department of Physics, L69 7ZE Liverpool, UK
[g] University of Athens, Department of Physics, GR-15771 Athens, Greece

Abstract

An intercomparison of the performances of active neutron detectors was carried out in pulsed neutron fields in the new HiRadMat facility at CERN. Five detectors were employed: four of them (two ionization chambers and two rem counters) are routinely employed in the CERN radiation monitoring system, while the fifth is a novel instrument, called LUPIN, specifically conceived for applications in pulsed neutron fields. The measurements were performed in the stray field generated by a proton beam of very short duration with momentum of 440 GeV/c impinging on a dump. The beam intensity was steadily increased during the experiment by more than three orders of magnitude, with an H*(10) due to neutrons at the detector reference positions varying between a few nSv per burst and a few µSv per burst. The aim of the experiment was to evaluate the linearity of the detector response in extreme pulsed conditions as a function of the neutron burst intensity. The results show that the ionization chambers have a quasi-linear response, very close to the ideal behaviour also for values of H*(10) of a few µSv/burst; the LUPIN response shows a slight deviation from the ideal curve when the H*(10) per burst is higher than 100 nSv; the rem counters response are characterized by a strong deviation from the linearity for H*(10) values higher than a few ten of nSv.

CERN, 1211 Geneva 23, Switzerland
22 May 2013

Submitted for publication in *Radiation Measurements*

1. Introduction

In the last decades radiation protection has been dealing with an increasing number of applications where PNF represent an important component of the stray radiation field, e.g. around particle accelerator facilities, plasma wake field accelerators and free electron laser facilities. It is well known that active neutron detectors can suffer severe limitations when used in these operating conditions. The limitations are due to electronics constraints, i.e. the finite resolutions of the counting system (dead time effects when counting high reaction rates) and physical reasons, e.g. the diminution of the gas multiplication factor of proportional counters during the detection of a neutron burst [1] and volume recombination effects for ionization chambers. A comprehensive study focused on the evaluation of the behaviour of active neutron detectors in PNF has been recently carried out by Caresana et al. [2].

This paper presents and discusses the results of a similar experiment conducted at the High Radiation to Materials (HiRadMat) facility at CERN [3], with a different set of detectors and under different conditions. The aim was to verify the response linearity of several neutron detectors in extreme pulsed conditions as a function of the neutron burst intensity. In fact, as stated in ref. [4], two of the four requirements for an ideal detector to be used in PNF[1] are the capability to withstand very high instantaneous neutron fluxes with little or no saturation and, at the same time, to correctly measure the intensity of a single neutron burst. This makes the response linearity a fundamental parameter in determining the suitability of a detector for use in PNF, as it quantifies its ability to meet these two requirements.

Five detectors were employed: a novel rem counter specifically conceived for applications in PNF, called LUPIN (Long-Interval, Ultra-wide dynamic, PIle-up free Neutron rem counter) [4-6], two commercial rem counters (a Thermo Scientific FHT 762 Wendi-2 and a FHT 752 BIOREM) and two ionization chambers (pressurised Argon and Hydrogen type) employed in the Radiation Monitoring System for Environment and Safety (RAMSES) [7] at CERN. Since most of the monitoring stations at CERN usually deal with pulsed stray fields, this experiment was also conceived to verify the performance of the RAMSES detectors in extreme conditions.

The measurements were performed in the new HiRadMat facility at CERN. The facility has been specially designed for conducting experiments in order to investigate the effects of high intensity pulsed radiation on materials. The detectors were exposed in the stray field generated by a proton beam of very short duration with momentum of 450 GeV/c impinging on the dump. The secondary neutrons produced in the dump scatter through a 50 m long concrete tunnel before reaching the detectors. In order to intercompare the detectors in five different positions a specially designed, remotely controlled, rotating support was designed and built.

The beam intensity could be altered by changing the number of pulses in the proton bunch, while preserving the beam structure. This allowed the detectors to be comprehensively tested up to extreme stray field intensities, and the non-linear aspects of their response analysed. The beam intensity was steadily increased during the experiment by more than three orders of magnitude, with an H*(10) due to neutrons varying between a few nSv/burst and a few µSv/burst. As a consequence of the scattering that the neutrons encounter on the concrete walls and the tunnel structures, the stray field at the detector positions contains a significant delayed neutron component. This allowed the detector response to be tested in a pulsed stray field, in which a slow contribution is also observed.

2. Materials and methods

2.1. The HiRadMat facility

HiRadMat is a newly constructed facility designed to provide high-intensity pulsed beams to an irradiation area where beam-to-material experiments can be performed. The facility has been constructed 35 m under the ground level at the already existing tunnel of the old CERN WANF Area [8]. The primary proton beam that reaches the irradiation area is extracted from the Super Proton Synchrotron (SPS). The nominal proton momentum is 440 GeV/c. The pulse consists of several bunches (from 1 up to 288, according to the user needs). The intensity of

[1] PNF = Pulsed Neutron Fields

each bunch can be varied from 10^9 up to $1.7 \cdot 10^{11}$ protons and the spacing between them from 25 ns up to 100 ns. That gives a maximum pulse intensity of $5 \cdot 10^{13}$ protons/spill and a maximum pulse length of 28.8 μs. The available beam line optics allow for a flexible spot size from 0.5 mm^2 up to 2 mm^2. A layout of the experimental area is shown in Figure 1, alongside with the code names of the tunnels.

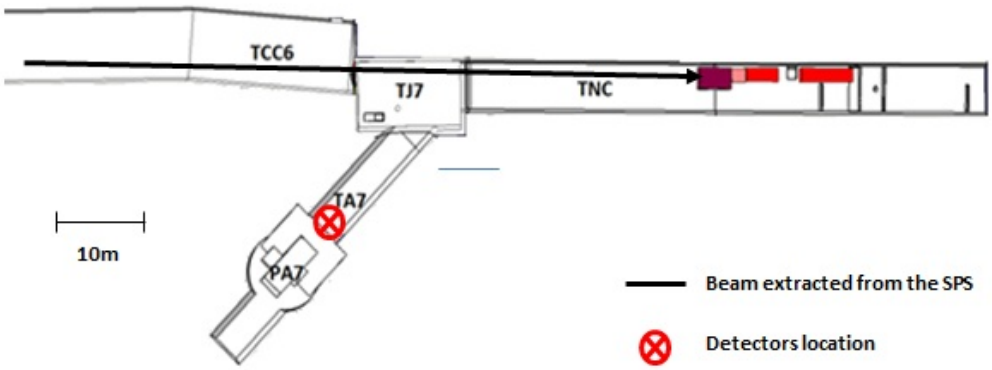

Figure 1 - Layout of the HiRadMat facility. The beam (black line) was impinging on the dump in the TNC tunnel, while the detectors were placed in the TA7 tunnel (red spot).

For the purposes of this experiment, the proton beam was impinging directly on the beam dump, while the detectors were placed in the TA7 tunnel, just after the air-tight ventilation door that separates the experimental area from the access area. The HiRadMat beam dump [9] (see Figure 2) consists of a cylindrical graphite core of a diameter of 8 cm and total length of 350 cm. The core is enclosed into a larger cylindrical case, made from a special alloy (97% Al, 2% Cu, 0.4 Zn, 0.35% Cr), with a diameter of 16 cm and a length of 350 cm. This case is further enclosed into a cylindrical copper case with the same length and a diameter of 32 cm. The structure is surrounded by blocks of marble, iron and stainless steel. In addition, in order to completely stop the charged particles (produced in the dump core) from contaminating the rest of the tunnel, additional 10.5 m of iron blocks are placed behind the dump.

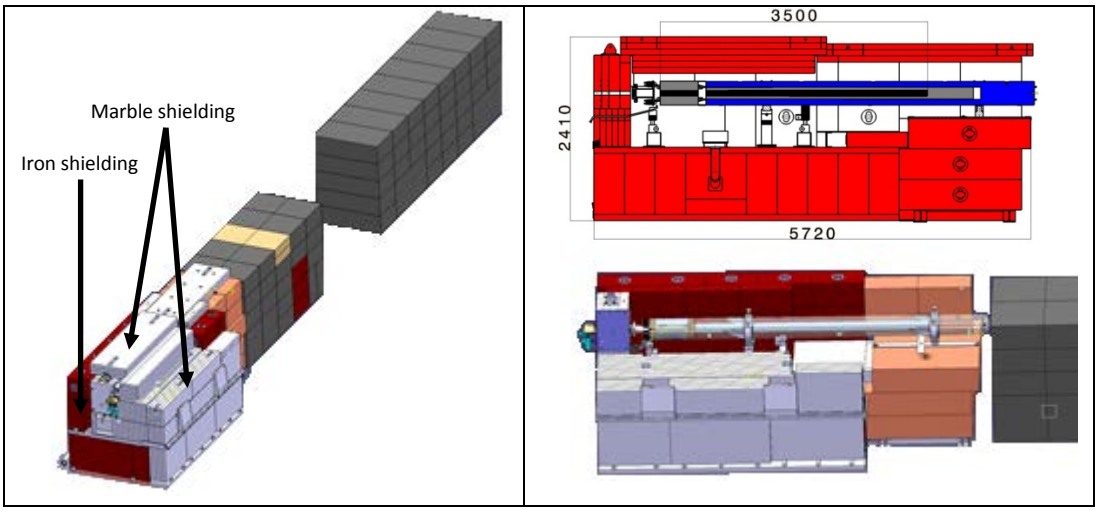

Figure 2 - The HiRadMat beam dump system. The carbon core of the dump is surrounded by marble and iron shielding.

A beam spot size of around 2 mm^2 and a bunch spacing of 50 ns were chosen. A list of the nominal intensities of the pulses to be extracted from the SPS and shot on the beam dump is shown in Table 1. These are the

nominal values, while during the measurements the obtained intensities were slightly different and, in some cases some settings had to be skipped. The beam intensity is measured via a monitor affected by a 3% uncertainty.

Table 1 - Nominal beam settings used during the experiment.

Setting number	Pulse intensity [protons on dump]
1	$5 \cdot 10^{9}$
2	10^{10}
3	$2 \cdot 10^{10}$
4	$4 \cdot 10^{10}$
5	$7.5 \cdot 10^{10}$
6	10^{11}
7	$2 \cdot 10^{11}$
8	$4 \cdot 10^{11}$
9	$7.5 \cdot 10^{11}$
10	10^{12}
11	$2 \cdot 10^{12}$
12	$4 \cdot 10^{12}$
13	$7.5 \cdot 10^{12}$

2.2. The detectors

2.2.1. LUPIN

The LUPIN is a prototype extended range rem counter available in two versions, using either a ^{3}He or BF_3 proportional counter. The counter is inserted in a spherical or cylindrical moderator with lead and cadmium inserts and uses front-end electronics based on a logarithmic amplifier. The working principle is simple: the current generated inside the proportional counter is amplified with a current to voltage logarithmic amplifier and the output voltage is acquired with an Analog to Digital Converter (ADC). The current is integrated over a user settable time window. The integrated charge divided by the charge expected by a single neutron interaction gives the number of neutrons occurring in a defined time. The output value in H*(10) is obtained by applying a proper calibration factor, expressed in nSv/interaction. The BF_3 version, shown in Figure 3, was employed for this experiment. The calibration, carried out in the CERN laboratory with a PuBe source with activity of 1.85 TBq, gave a factor of 0.480 nSv/interaction. Figure 4 shows the response function as simulated via the MCNPX [10] code.

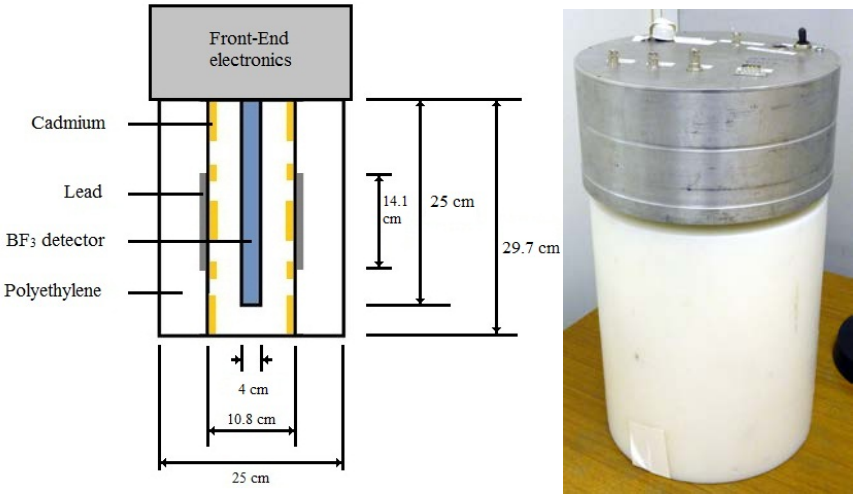

Figure 3 - Geometry (left) and picture (right) of the BF_3 version of the LUPIN.

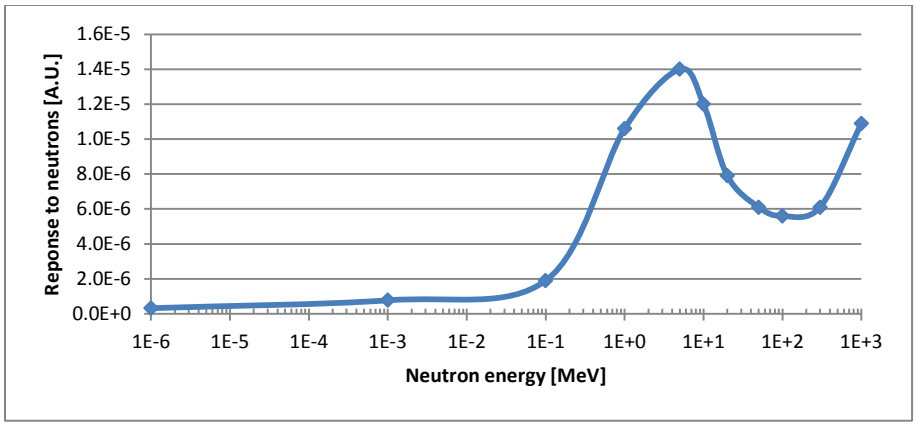

Figure 4 - Response function to neutrons of the BF_3 version of the LUPIN.

2.2.2. Thermo Scientific FHT 752 (BIOREM)

The Thermo Scientific FHT 752 BIOREM (Figure 5) is a commercial neutron dose rate meter for stationary and portable use, especially suited for environmental measurements. It employs a BF_3 proportional counter placed in a cylindrical moderator containing polyethylene and boron carbide. The output is given in H*(10), but an internal calibration factor, expressed in nSv/count, can be set by the user. The calibration carried out at CERN resulted in a calibration factor of 0.550 nSv/count. The response function is given in Figure 6.

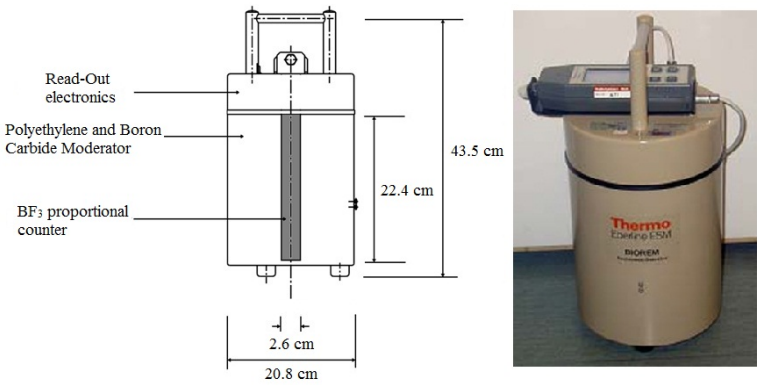

Figure 5 – Geometry (left) and picture (right) of the BIOREM.

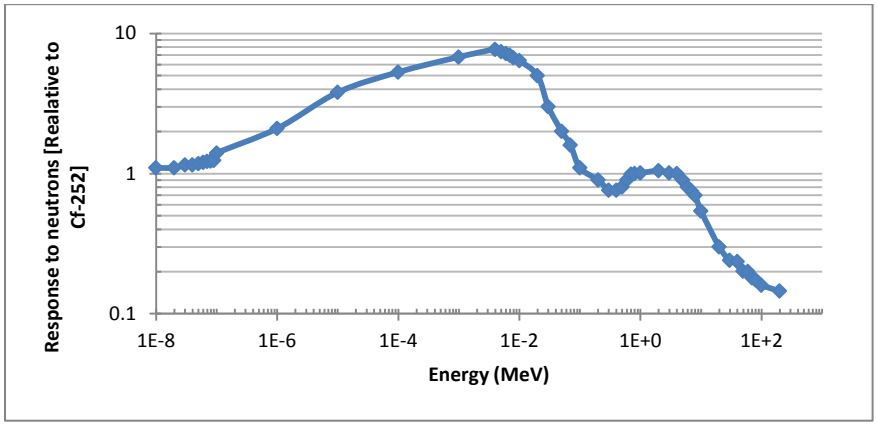

Figure 6 - Response function to neutrons of the BIOREM, expressed in units relative to the response of moderated ^{252}Cf [11].

2.2.3. Thermo Scientific FHT 762 (Wendi-2)

The Thermo Scientific FHT 762 Wide Energy Neutron Detection Instrument (Wendi-2) is a commercial extended range rem counter designed to measure the H*(10) rate within an energy range from thermal up to 5 GeV [12]. It consists of a ^{3}He proportional counter surrounded by a cylindrical polyethylene moderator assembly and a layer of tungsten powder. This additional layer of high-Z material enhances the detector response to high-energy neutrons via inelastic scattering interactions [13, 14]. The geometry of the detector is shown in Figure 7. The output is given in H*(10), but the internal calibration factor can be changed by the user. The calibration carried out at CERN resulted in a calibration factor of 0.320 nSv/count. The response function of the detector is shown in Figure 8.

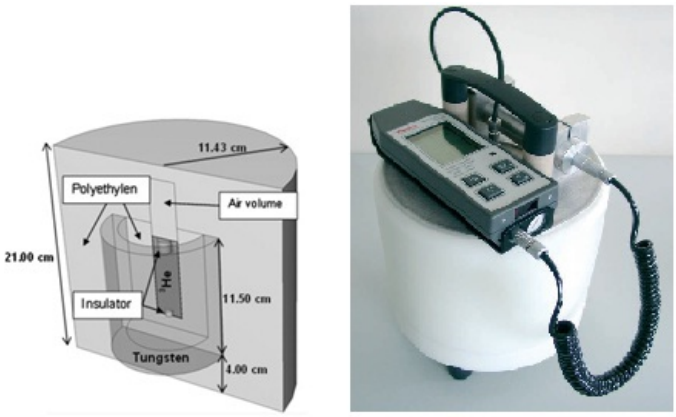

Figure 7 – Geometry [12] (left) and picture (right) of the Wendi-2.

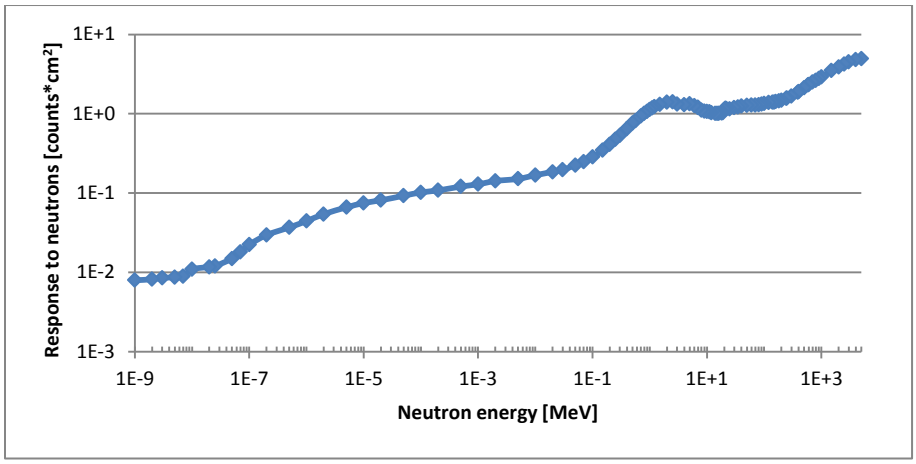

Figure 8 – Response function to neutrons of the Wendi-2 [12].

2.2.4. Hydrogen-filled Ionization Chamber

The Hydrogen-filled ionization chamber used for RAMSES is a customised Centronic IG5-H20. It is designed for use in mixed radiation fields, and is capable of detecting high-energy charged particles, photons and neutrons. The Hydrogen is pressurised to 20 bars ($2{\cdot}10^{6}$ Pa). The energy range of the chamber is 65 keV up to 10 MeV and the measuring range is 1 µGy/h up to 10 Gy/h [15]. A charge digitizer converts the charge created in the active volume to TTL pulses, which can be collected by digital data acquisition cards. To convert the output signal into H*(10), a calibration factor, expressed in nSv/pC or nSv/count, must be applied. This is calculated for each monitoring station according to the expected neutron and gamma spectra in the area. The calculation is done by folding the response function of the detector (shown in Figure 9 for the neutron component only) with the spectra known experimentally or obtained via MC simulations.

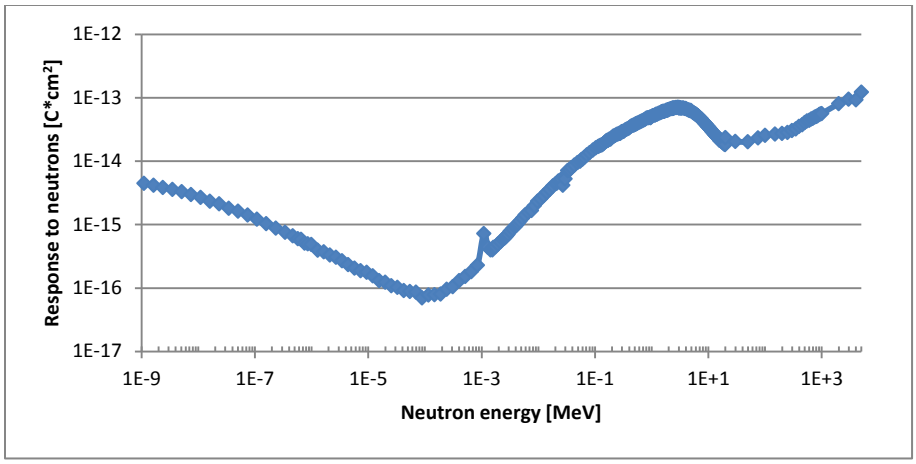

Figure 9 – Response function to neutrons of the Hydrogen-filled ionization chamber [16].

2.2.5. Argon-filled Ionization Chamber

The Argon-filled ionization chamber used for RAMSES is a customised Centronic IG5-A20 ionization chamber. The Argon is pressurised to 20 bars ($2 \cdot 10^6$ Pa) and has a measuring range from 100 nSv/h to 10 Sv/h. It is designed for the detection of photons or minimal ionising particles, over an energy range of 50 keV up to 10 MeV. The geometry of the chamber, which is very similar to the IG-H20, is shown in Figure 10. The analysis of the signal is the same as for the IG5-H20 chamber [15]. Figure 11 shows the response function to neutrons.

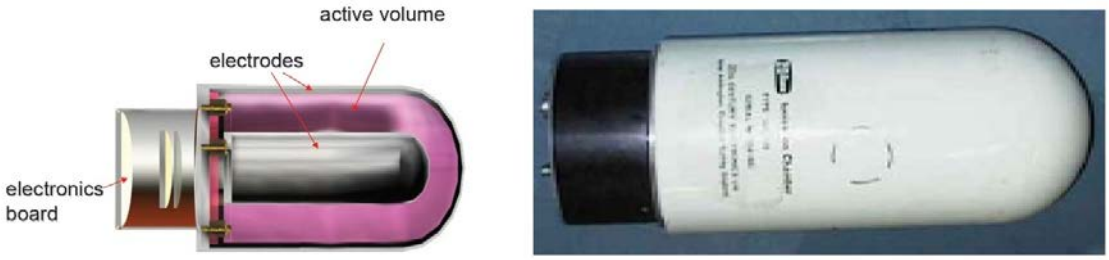

Fig 10 – Geometry [16] (left) and picture (right) of the IG5 ionization chamber. The active gas can be either H or Ar, giving the two versions used in this paper.

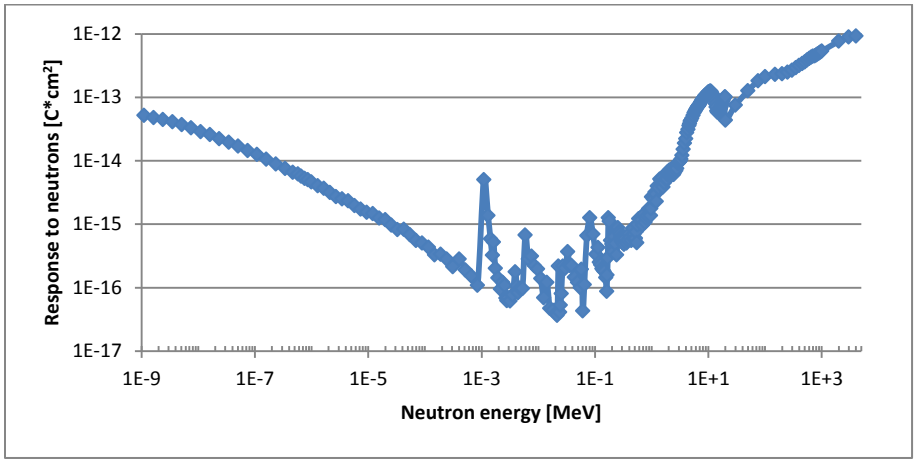

Figure 11 - Response function to neutrons of the Argon-filled ionization chamber [16].

2.3. Experimental set up

The detectors were tested at the end of the TA7 tunnel (see Figure 1). In this area the stray radiation field is only due to neutrons since it is at a distance of 50 m from the dump and the photon component is strongly attenuated, while the neutrons scatter towards the wall and the floor of the tunnel. In a test run carried out before the main series of measurements, it was verified that the radiation gradient in the area is quite high (30% difference in the measured H*(10) between two positions 2 m from one another [17]). Due to the radiation gradient, and given the difficulty to access the measurement area, it was decided to build a rotating support for the five detectors that could be remotely controlled. This solution allowed testing each detector in 5 positions, so as to have a comparison of the responses in the same conditions of stray field with good reproducibility. Moreover, since no access to the experimental area is allowed when SPS is filling the LHC, the number of accesses had to be limited. With this solution the accesses to the area were limited to one before the experiment in order to install the equipment and one after the measurements for dismantling.

2.3.1. The rotating support

The support has been designed in the form of a Ferris wheel, with five supports, each one attached to the skeleton in such a way that, as the wheel turns, the supports are kept upright by gravity. The skeleton is welded onto a central axis. This axis is supported by two vertical beams which are welded on a base plate, mounted for stability on two horizontal beams. The support was entirely built out of aluminium to minimize the total weight as well as to limit activation issues. A rotary motor makes the entire assembly rotate with a transmission belt while an encoder gives information on the absolute angular position [18]. The overall set-up could be checked on-line via a web camera installed next to the wheel. The distance between the five supports was maximized (being limited by the height of the tunnel ceiling) in order to reduce cross-interferences between the detectors. The configuration scheme and a picture with the detectors mounted on the wheel are shown in Figure 12.

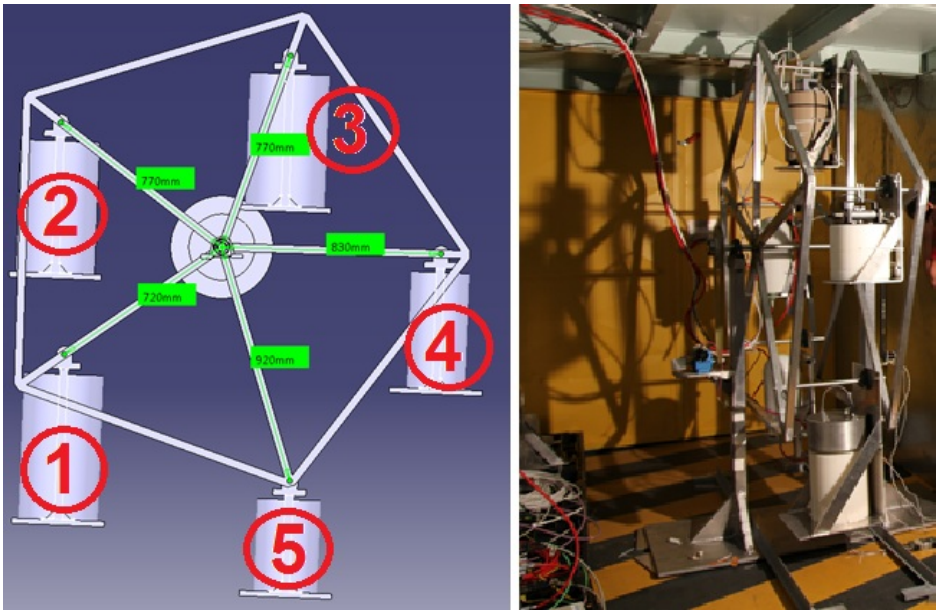

Figure 12 - Technical Drawing (left) and photograph (right) of the rotating support installed in the facility. The arbitrary numbers given to identify the positions are also shown.

2.4. Data acquisition

The data acquisition for the four detectors used in RAMSES was carried out according to the standard procedure that is followed for all the CERN monitoring stations. The data from the detectors is gathered every second in a local electronics station, which processes and sends them via an Ethernet connection, available in the

experimental area, to the central server. The data is afterwards retrieved for the off-line analysis from the RAMSES database. The time was synchronised during the measurements with the server time and recorded. Both the detectors and the local station were connected to a power supply.

The signal of the LUPIN was partially processed by the front-end electronics (internally powered by a battery) and then output to a Bayonet Neill Concelman (BNC) cable. A custom made cable allowed for the signal to be delivered to the HiRadMat control room on the surface, where the output was connected to a Personal Computer (PC) oscilloscope (PicoScope 4424 by PicoTechnology), which in turn was connected to a portable computer. The data was monitored on-line by a LabVIEW® program, acquired at a frequency of 5 MHz and stored on log-files for the off-line analysis.

3. Results

3.1. FLUKA simulations

Monte Carlo simulations were carried out with the FLUKA code [19, 20] (version 2012.2.17) to calculate the neutron energy distributions at the end of the TA7 tunnel, where the detectors were installed. A detailed geometry model of the tunnel civil engineering structures, the beam dump and the basic electromechanical equipment of the HiRadMat access and experimental area [21] were implemented in FLUKA, together with the neutron detectors. A figure of the model visualised using the FLAIR interface [22] is shown in Figure 13.

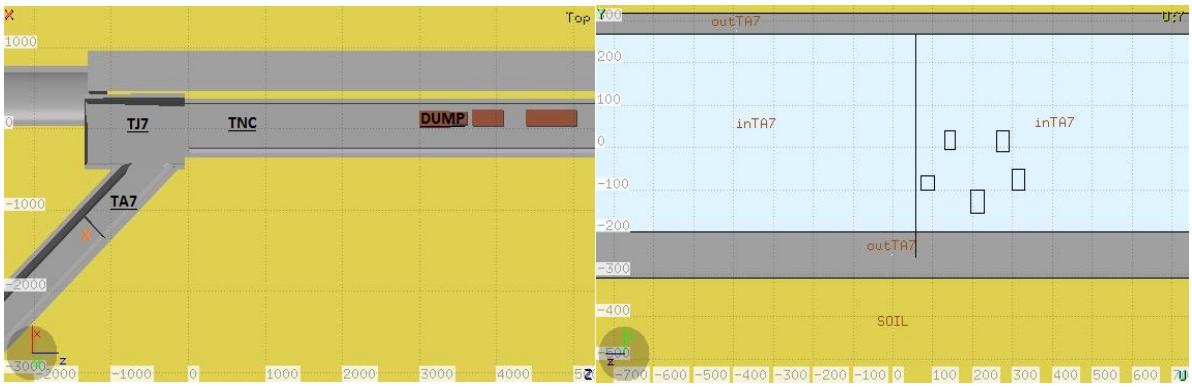

Fig 13 - The geometry model implemented for the FLUKA simulations. a) Top-view of the facility: the rotating support is marked with a red letter "X". b) Side-view of the TA7 tunnel: the detectors are placed after the ventilation door.

The primary proton beam, with a nominal momentum of 440 GeV/c and a Gaussian shape with a spot size of 2 mm, was simulated to impinge on the dump. Since the dump core consists of 350 cm of graphite, whose nuclear interaction length is 38.8 cm, all the protons interact with the graphite, producing a hadronic cascade and an electromagnetic shower. The simulated prompt neutron spectrum produced at the dump, which is backscattered towards TJ7, was scored 2 m upstream of the dump core (Figure 14).

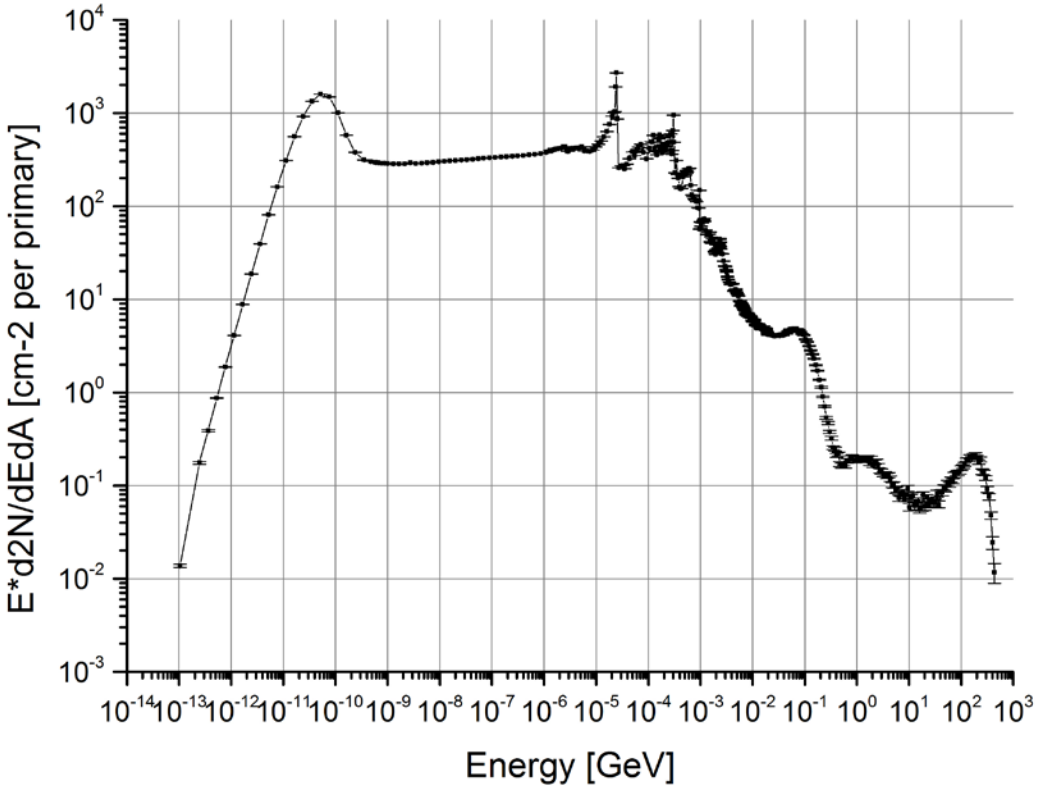

Figure 14 - Simulated backscattered neutron spectrum at 2 m upstream of the beam dump, in isolethargic view. The results are normalized per primary proton.

The neutron spectrum consists of five components: a thermal part, due to neutron elastic scattering interactions on the iron and marble structures of the dump as well as on the concrete walls of the tunnel; an intermediate region from 10 eV up to 1 MeV; an evaporation component, caused by the particle-nucleus quasi-elastic interactions with most probable energy in the MeV region; a high energy component (> 10 MeV) due to particle-nucleon high-energy interactions. Since the p-n cross section of most shielding materials (like iron and concrete) reaches a minimum at about 100 MeV, the appearance of this maxwellian-shaped high-energy peak occurs in our case around this energy value. Finally, the very high energy part (> 10 GeV) comes from the backscattering of high energy neutrons produced inside the dump.

The thermal and evaporation neutrons are dominating the spectrum, while the high energy component is around three orders of magnitude lower. In fact high energy neutrons produced in the dump are mainly forward peaked, while only a very small portion is backscattered at 180º. These backscattered neutrons continue travelling and scattering through the TNC, TJ7 and TA7 tunnels. The simulated neutron spectra that finally reach the detectors are shown in Figure 15.

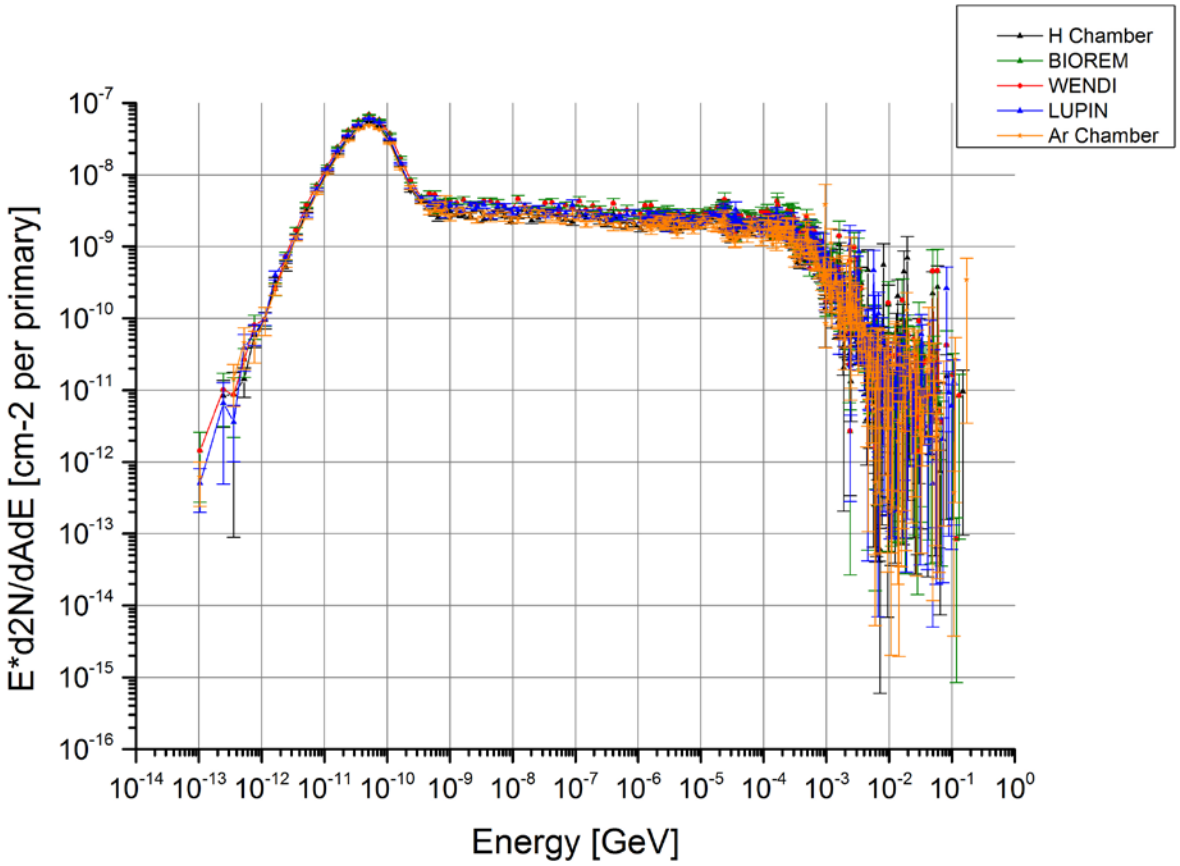

Figure 15 - The simulated neutron spectra at each of the detector reference positions. The plot is in isolethargic view. The results are normalized per primary proton.

The shape of the neutron spectrum reaching the detectors is significantly different from the one produced near the dump. The thermal component is the one that dominates the neutron spectral fluence, since the intermediate and high energy neutrons produced in the dump are backscattered on the tunnels floor and walls for 50 m (total distance between the detectors and the beam dump). Therefore, a significant portion of the intermediate energy neutrons (from tens of eV up to a few hundred keV) produced in the dump loses a significant part of their energy. Additionally, since the TA7 tunnel has an angle of 45º with respect to TNC, the majority of the backscattered intermediate and high energy neutrons from the beam dump follow a straight course and escape through the TJ7 and TCC6 tunnels (see Figures 1). This accounts for the decrease of about six orders of magnitude in the total number of neutrons between the position near the dump and the detector positions. At the same time, this explains the strong reduction of the evaporation peak at 1 MeV (which is instead clear in Figure 14). The statistical uncertainties for energies higher than 1 MeV are very high, since the number of neutrons reaching the detectors in this energy region is very limited.

The arrival time distribution of the neutrons at the detector reference positions was also simulated. The results are shown in Figure 16. The distribution is divided in three parts according to the neutron energy.

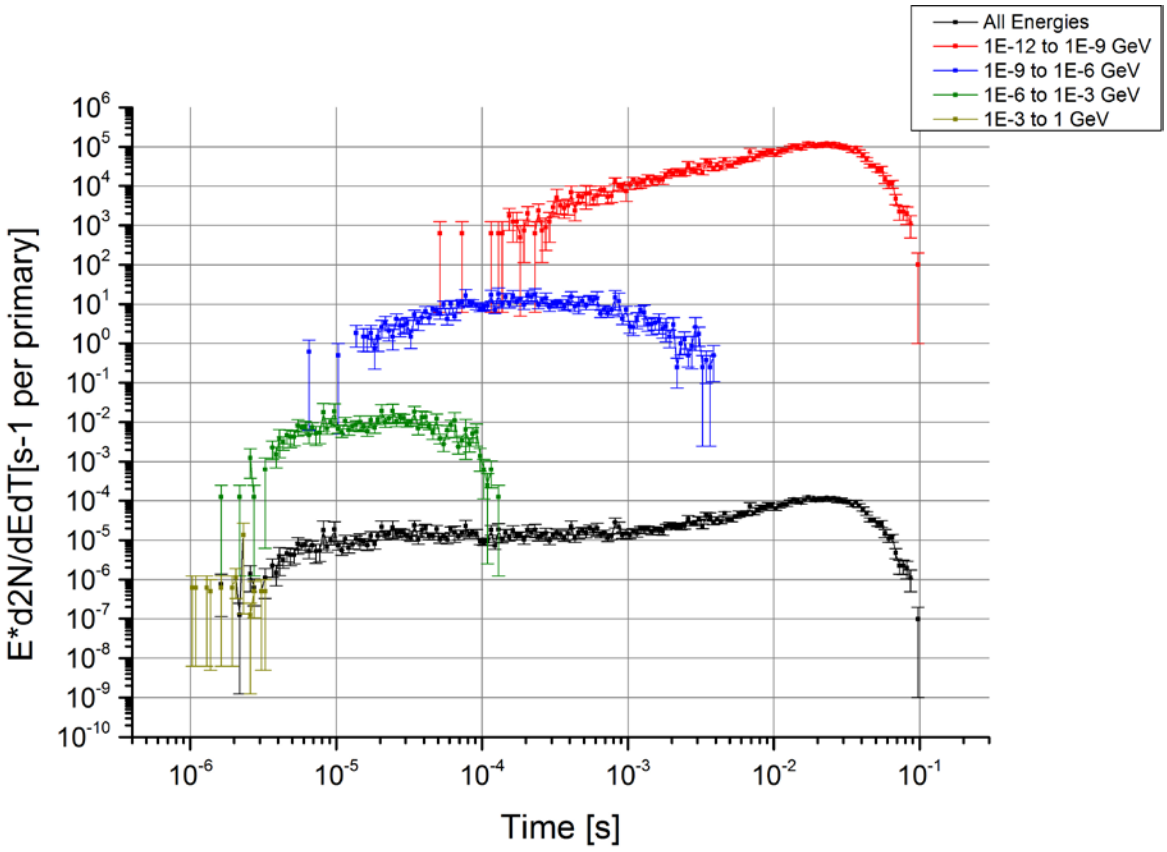

Figure 16 - The simulated time distribution of the neutrons at the detector reference positions. The green, blue and pink plots represent the low, medium and high energy components, respectively. The red plot, differently scaled for better visualization, is the sum of all the components. The beam impinges on the dump at t = 0.

As expected, the high energy component of the field (i.e. the one with the higher velocity) is the first which is reaching the detectors. The last neutrons arrive about 100 ms after the beam impinged on the dump.

3.2. Detector calibrations

Since the aim of the experiment is to check the linearity of the response of the detectors, the focus is not on the match between the simulated values of H*(10) per primary and the measured ones. Nevertheless, it was decided, when possible, to set the calibration factor of the detector taking into account the expected neutron spectra and the H*(10) per primary as simulated via FLUKA in the five measuring positions. The process followed to set the proper calibration factor is explained below for each detector.

Where the folding between the response function of the detector and the simulated spectrum was not possible, the calibration factor obtained in the CERN laboratory with the PuBe source was kept. It should be noted that this value is affected by an uncertainty of 7%, as reported in the calibration certificate of the source. At the same time, where the folding was possible, the calculated factors are affected by two contributions of uncertainty: the first on the response function, the second on the simulated spectrum, both calculated via Monte Carlo codes. However, it was decided not to take into account any kind of uncertainty for two reasons: firstly, because these are correlated uncertainties, which are the same for all the detectors (in fact all of them were calibrated with the same source and/or folded with the same simulated neutron spectra); secondly, because this would not have improved the check of the response linearity.

3.2.1. LUPIN

Since the response function of the detector is still known only in arbitrary units (the detector is under characterization) and for a limited number of energies (see Figure 4), it was decided to use the PuBe calibration factor determined in the CERN calibration laboratory. However, the simulated spectral fluence is slightly different from the PuBe one, being characterized by a peak at thermal energy and a rapid drop for energies higher than 100 keV. A comparison of the two spectra is shown in Figure 17.

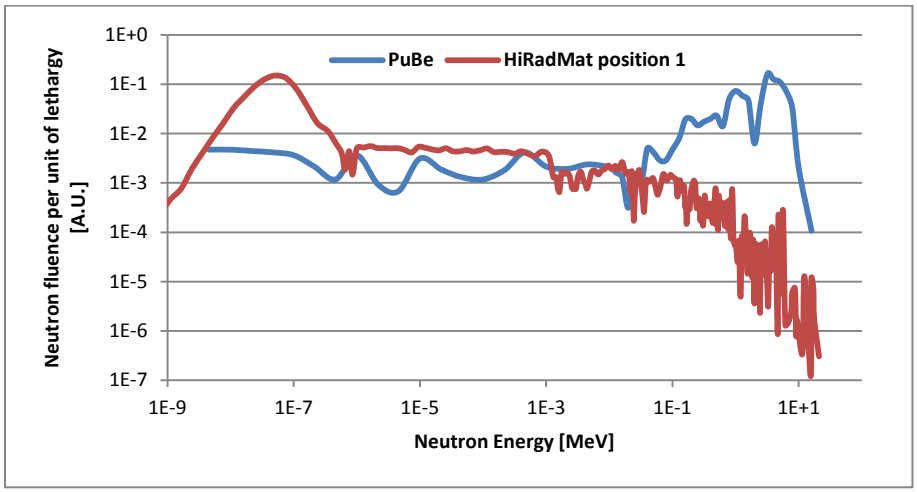

Figure 17 – Comparison of the neutron spectrum of the PuBe source of the CERN calibration laboratory and the one expected in HiRadMat measuring position 1. The spectra have been normalized (integrated area below the spectra equal to 1) and are given in arbitrary units.

3.2.2. BIOREM FHT 752

The response function of the detector is known in units relative to the response of a source of moderated ^{252}Cf. However the sensitivity of the detector to this neutron field is unknown and the response function itself is not accurately known for thermal energies, i.e. where the simulated spectra have a huge peak. Therefore it was decided not to modify the calibration factor obtained with the PuBe source.

3.2.3. Wendi-2

For the Wendi-2 the response function is well known for the entire neutron energy spectrum. This function was folded with the simulated neutron spectrum for each measuring position to derive the expected number of counts per primary. The expected value of H*(10) per primary (expressed in nSv/primary) simulated via FLUKA was then employed to obtain the best calibration factor to be used (nSv/count). However, this value has been found to be equal in all the positions to the one obtained in the calibration laboratory, i.e. 0.32 nSv/count.

3.2.4. Hydrogen and Argon-filled Ionization Chamber

For both RAMSES ionization chambers the response function to neutrons is well known. Therefore the same procedure used to derive the Wendi-2 calibration factor was used, except for the fact that the values are expressed in terms of unit of charge and not counts. The results for the five positions are given in Table 2.

Table 2 - Calibration factors used for the RAMSES Hydrogen-filled and Argon-filled ionization chambers in the five measuring positions. All the values are in nSv/pC.

Hydrogen-filled ionization chamber				
Position 1	Position 2	Position 3	Position 4	Position 5
3.77	3.85	3.81	3.76	3.78
Argon-filled ionization chamber				
Position 1	Position 2	Position 3	Position 4	Position 5
6.52	6.61	6.62	6.24	6.44

3.3. Detector data

The results of the measurements are shown in Tables 3-7. All the values refer to the integrated H*(10) detected in the stray field generated by a single beam pulse impinging on the dump. The uncertainty corresponds to the statistical one for the LUPIN, the BIOREM and the Wendi-2. For the ionization chambers (for which it is not possible to derive a statistical uncertainty) the global uncertainty has been set equal to 1%: this includes possible changes in the gas sensitivity due to variation in the temperature during the experiment and minor uncertainties on the electronic components of the analysing circuit as given by the manufacturer [23]. Since the aim of the experiment was to check the response linearity, the uncertainty on the positioning was neglected. In fact this would have affected only the comparison between data acquired with different detectors in the same position.

The beam settings refer to the nominal values listed in Table 1. Some of them are named with a letter as a suffix (e.g. setting 8a and 8b) because different measurements were carried out with the same beam setting (even if beam intensities were not exactly reproducible). The expected H*(10) was calculated by applying to the beam intensity a coefficient, expressed in nSv per proton on dump, derived from the linear region of the LUPIN and the two ionization chambers, i.e. at low beam intensities, where saturation effects are not present. The coefficients used for the five positions are shown in Table 8. The values of expected H*(10) are affected by two sources of uncertainties: 3% derived from the uncertainty on the beam intensity; 5% due to the uncertainty on the coefficients. However these uncertainties are not given in Tables 3-7 for simplicity.

Table 3 – Results of the measurements in position 1, with uncertainties in parenthesis.

	LUPIN	H Chamber	Ar Chamber	Wendi-2	BIOREM
Beam setting	Expected/measured H*(10) [nSv]	Expected/measured H*(10) [nSv]	Expected/measured H*(10) [nSv]	Expected/measured H*(10) [nSv]	Expected/measured H*(10) [nSv]
1a	3.9 / 3.4 (1.3)	3.2 / 2.7 (0.1)	4.4 / 5.5 (0.1)	4.6 / 3.9 (1.1)	5.2 / 4.4 (1.6)
1b	4.4 / 3.4 (1.3)	5.2 / 5.4 (0.1)		6.3 / 5.3 (1.3)	
2a	7.9 / 6.2 (1.7)	6.6 / 6.3 (0.1)	7.8 / 9.7 (0.1)	7.8 / 5.3 (1.3)	
2b	10.3 / 9.6 (2.2)	8.5 / 8.0 (0.1)		7.9 / 6.0 (1.4)	
3a	16.1 / 13.0 (2.5)	15.2 / 12.3 (0.1)	15.1 / 14.6 (0.1)	15.9 / 8.2 (1.6)	16.7 / 13.1 (2.7)
3b	17.6 / 15.4 (2.7)	19.2 / 17.9 (0.2)	17.0 / 17.5 (0.1)	17.9 / 8.5 (1.6)	
4a	37.2 / 32.2 (3.9)	40.9 / 34.6 (0.3)		31.4 / 13.8 (2.1)	
5	61.8 / 41.8 (4.5)			59.8 / 15.3 (2.2)	
6a	84.5 / 64.3 (5.6)	76.7 / 62.3 (0.6)		83.4 / 19.9 (2.5)	
6b		87.1 / 78.4 (0.8)		85.7 / 23.4 (2.7)	
7a	166.2 / 152.6 (8.6)	162.0 / 126.6 (1.3)			179.4 / 77.8 (6.5)
7b		200.3 / 169.0 (1.7)			
8a	365.8 / 278.9 (11.6)	409.4 / 353.3 (3.5)	345.8 / 335.1 (3.4)	348.4 / 55.1 (4.2)	331.0 / 114.7 (7.9)
8b					357.1 / 120.8 (8.2)
10a	871.0 / 587.0 (16.8)	905.8 / 756.4 (7.6)	871.0 / 845.4 (8.5)	897.1 / 97.8 (5.6)	905.8 / 220.8 (11.0)
11a			905.8 / 862.1 (8.6)	940.7 / 107.8 (5.9)	1785.6 / 320.8 (13.3)
11b	1750.7/ 1012.3 (22.0)	1742 / 1451.7 (14.5)		1794.3 / 146.8 (6.9)	1820.4 / 341.9 (13.7)
12a	3579.8 / 1778.4 (29.2)	3579.8 / 2951.4 (29.5)	3510.1 / 3275.5 (32.8)	3719.2 / 226.3 (8.5)	3675.6 / 506.9 (16.7)
12b			3623.4 / 3429.3 (34.3)		3710.5 / 499.7 (16.6)
13a	6863.5 / 2719.2 (36.1)	6924.5 / 5742.8 (57.4)	6793.8 / 5232.5 (52.3)	6576.1 / 293.3 (9.7)	6933.2 / 691.7 (19.5)
13b	6959.3 / 2792.2 (36.6)	6968.0 / 5765.7 (57.7)		6985.4 / 298.3 (9.8)	6985.4 / 691.7 (19.5)

Table 4 – Results of the measurements in position 2, with uncertainties in parenthesis.

	LUPIN	H Chamber	Ar Chamber	Wendi-2	BIOREM
Beam setting	Expected/measured H*(10) [nSv]	Expected/measured H*(10) [nSv]	Expected/measured H*(10) [nSv]	Expected/measured H*(10) [nSv]	Expected/measured H*(10) [nSv]
1a	3.2 / 1.9 (1.0)	3.0 / 2.7 (0.1)		2.7 / 2.2 (0.8)	2.4 / 2.2 (1.1)
1b					3.3 / 2.7 (1.2)
2a	4.1 / 3.8 (1.4)	4.3 / 4.3 (0.1)	4.0 / 4.4 (0.1)	4.8 / 2.2 (0.8)	4.1 / 3.8 (1.4)
2b		4.9 / 4.8 (0.1)	6.3 / 7.4 (0.1)		5.3 / 4.4 (1.6)
2c					5.9 / 5.5 (1.7)
3a	10.3 / 8.6 (2.0)	9.5 / 9.8 (0.1)	10.0 / 10.7 (0.1)	9.3 / 5.8 (1.4)	9.7 / 7.7 (2.1)

3b	11.7 / 9.1 (2.1)	11.1 / 9.5 (0.1)	10.9 / 11.1 (0.1)	10.5 / 6.8 (1.5)	
4a		20.8 / 16.3 (0.2)	22.9 / 24.7 (0.2)		25.2 / 19.2 (3.2)
4b		21.5 / 18.8 (0.2)			
5		38.3 / 29.5 (0.3)	38.1 / 40.3 (0.4)		47.8 / 29.0 (4.0)
6a		52.8 / 44.4 (0.4)	51.0 / 54.9 (0.5)		59.1 / 33.4 (4.3)
6b					118.1 / 55.9 (5.5)
7a	110.6 / 73.9 (6.0)				
8a	204.1 / 168.5 (9.0)	214.8 / 178.3 (1.8)	119.5 / 131.4 (1.3)	213.2 / 41.7 (3.7)	236.3 / 87.6 (6.9)
8b			230.4 / 252.8 (2.5)		
9		553.1 / 480.2 (4.8)			
10a	558.5 / 407.5 (14.0)	1106.2 / 932.4 (9.3)	537.0 / 544.6 (5.4)	537.0 / 68.4 (4.7)	558.5 / 158.3 (9.3)
10b				558.5 / 66.2 (4.6)	
11	1100.9 / 699.4 (18.3)		1090.1 / 1136.4 (11.4)		1074.0 / 224.2 (11.1)
12a	2266.1 / 1015.2 (22.1)	2293.0 / 1863.2 (18.6)	2207.1 / 2346.6 (23.5)	2164.1 / 159.1 (7.1)	2207.1 / 361.4 (14.1)
12b		2303.7 / 1883.6 (18.8)	2255.4 / 2364.9 (23.6)		
13a	4274.5 / 1315.2 (25.1)	4054.4 / 3295.7 (33.0)	4231.6 / 4423.2 (44.2)	4188.6 / 220.8 (8.4)	4269.2 / 513.3 (16.8)
13b	4306.7 / 1722.2 (28.8)	4306.7 / 3506.2 (35.1)	4290.6 / 4500.3 (45.0)	4215.5 / 225.1 (8.5)	

Table 5 – Results of the measurements in position 3, with uncertainties in parenthesis.

	LUPIN	H Chamber	Ar Chamber	Wendi-2	BIOREM
Beam setting	Expected/measured H*(10) [nSv]	Expected/measured H*(10) [nSv]	Expected/measured H*(10) [nSv]	Expected/measured H*(10) [nSv]	Expected/measured H*(10) [nSv]
1a	2.4 / 2.4 (1.1)	3.3 / 2.5 (0.1)	2.6 / 4.0 (0.1)	2.2 / 1.4 (0.7)	2.9 / 3.3 (1.3)
1b				3.3 / 2.8 (0.9)	
2a	4.6 / 3.4 (1.3)			5.6 / 3.2 (1.0)	4.7 / 4.9 (1.6)
2b				6.2 / 4.3 (1.2)	6.1 / 4.9 (1.6)
3a	10.0 / 7.7 (1.9)	9.9 / 8.6 (0.1)	9.0 / 8.8 (0.1)	8.8 / 6.0 (1.4)	9.5 / 6.0 (1.8)
3b		11.1 / 9.2 (0.1)	10.6 / 11.2 (0.1)	10.8 / 6.4 (1.4)	
4a			19.9 / 21.2 (0.2)	24.1 / 9.6 (1.8)	21.9 / 15.3 (2.9)
5			36.6 / 37.1 (0.4)	45.7 / 13.1 (2.0)	36.4 / 21.3 (3.4)
6a			50.5 / 52.9 (0.5)	51.3 / 18.8 (2.5)	49.8 / 29.0 (4.0)
7a		105.7 / 97.8 (1.0)		95.4 / 24.1 (2.8)	97.9 / 53.1 (5.4)
7b				112.9 / 27.7 (3.0)	
8a	203.7 / 169.0 (9.0)	210.3 / 193.4 (1.9)	205.2 / 185.9 (1.9)	225.7 / 45.1 (3.8)	215.5 / 75.6 (6.4)
10a	513 / 395.0 (13.8)		528.4 / 605.4 (6.1)	533.5 / 65.0 (4.6)	513.0 / 143.9 (8.9)
10b	533.5 / 457.9 (14.8)	533.5 / 488.6 (4.9)			
11a		1051.7 / 938.6 (9.4)	1056.8 / 961.7 (9.6)	1026.0 / 106.7 (5.8)	1031.1 / 234.9 (11.4)
11b		1072.2 / 962.3 (9.6)			
12a	2067.4 / 1472.2 (26.6)	2164.9 / 1931.3 (19.3)	2200.7 / 2375.8 (23.8)	2108.4 / 150.3 (6.9)	2154.6 / 338.9 (13.7)
12b		2185.4 / 1938.0 (19.4)			
13a	4001.4 / 1869.1 (30.0)	4083.5 / 3620.6 (36.2)	4114.3 / 4437.2 (44.4)	4078.4 / 219.9 (8.4)	4042.4 / 493.3 (16.5)
13b		4114.3 / 3664.1 (36.6)			

Table 6 – Results of the measurements in position 4, with uncertainties in parenthesis.

	LUPIN	H Chamber	Ar Chamber	Wendi-2	BIOREM
Beam setting	Expected/measured H*(10) [nSv]	Expected/measured H*(10) [nSv]	Expected/measured H*(10) [nSv]	Expected/measured H*(10) [nSv]	Expected/measured H*(10) [nSv]
1a	2.6 / 3.4 (1.3)	3.5 / 3.1 (0.1)	4.1 / 4.9 (0.1)	3.1 / 3.1 (1.0)	3.7 2.7
1b	3.0 / 4.3 (1.4)		4.5 / 5.0 (0.1)	3.9 / 3.4 (1.0)	3.8 3.3
1c	4.1 / 3.8 (1.4)				
2a	6.8 / 6.7 (1.8)			6.3 / 4.5 (1.2)	5.5 / 6.0 (1.8)
2b	9.8 / 8.2 (2.0)			8.0 / 5.9 (1.4)	
3a	11.8 / 10.1 (2.2)	11.9 / 12.6 (0.1)	13.3 / 13.1 (0.1)	12.8 / 6.9 (1.5)	12.1 / 14.8 (2.9)
3b	12.1 / 9.1 (2.1)	13.5 / 10.2 (0.1)	15.0 / 14.3 (0.1)	13.9 / 7.9 (1.6)	
3c	15.2 / 13.9 (2.6)				
4a	32.4 / 30.2 (3.8)			29.5 / 12.0 (2.0)	26.8 / 13.1 (2.7)
5				49.0 / 17.2 (2.3)	47.3 / 19.7 (3.3)

6a	60.8 / 52.3 (5.0)			66.9 / 17.5 (2.4)	66.1 / 33.4 (4.3)
6b	69.0 / 64.3 (5.6)				67.9 / 34.5 (4.4)
7a	128.3 / 107.0 (7.2)		142.1 / 133.4 (1.3)	153.6 / 31.3 (3.2)	
7b	151.8 / 122.9 (7.7)				
7c	158.7 / 129.1 (7.9)				
8a	303.6 / 237.1 (10.7)	273.9 / 233.5 (2.3)	262.2 / 238.9 (2.4)	289.8 / 44.0 (3.8)	276.0 / 104.3 (7.6)
8b	324.3 / 260.6 (11.2)				
10	717.6 / 495.8 (15.4)	690.0 / 602.2 (6.0)	717.6 / 677.4 (6.8)	690.0 / 80.3 (5.1)	745.2 / 184.3 (10.1)
11a	1380.0 / 854.9 (20.3)		1414.5 / 1334.0 (13.3)	1386.9 / 116.7 (6.1)	1421.4 / 297.5 (12.8)
11b	1400.7 / 860.6 (20.3)		1442.1 / 1209.5 (12.1)		
12a	2835.9 / 1479.8 (26.7)	2780.7 / 2371.8 (2.4)	2911.8 / 2761.2 (27.6)	2835.9 / 176.9 (7.5)	2946.3 / 432.2 (15.4)
12b		2870.4 / 2438.0 (24.4)	2939.7 / 2780.3 (27.8)		2960.1 / 441.9 (15.6)
13a	5485.5 / 2417.0 (34.1)	5382.0 / 4533.1 (45.3)	5492.4 / 5217.3 (52.2)	5437.2 / 245.8 (8.9)	5209.5 / 601.7 (18.2)
13b	5520.0 / 2419.0 (34.1)	5416.5 / 4570.0 (45.7)	5533.8 / 5243.3 (52.4)		5533.8 / 625.0 (18.5)

Table 7 – Results of the measurements in position 5, with uncertainties in parenthesis.

	LUPIN	H Chamber	Ar Chamber	Wendi-2	BIOREM
Beam setting	Expected/measured H*(10) [nSv]	Expected/measured H*(10) [nSv]	Expected/measured H*(10) [nSv]	Expected/measured H*(10) [nSv]	Expected/measured H*(10) [nSv]
1a	4.0 / 4.3 (1.4)	3.6 / 3.8 (0.1)	3.0 / 3.4 (0.1)	4.4 / 3.9 (1.1)	
1b			3.5 / 4.9 (0.1)	5.2 / 5.3 (1.3)	
1c			4.1 / 5.7 (0.1)		
1d			5.0 / 6.2 (0.1)		
1e			5.7 / 6.6 (0.1)		
2a	7.3 / 8.2 (2.0)	6.0 / 5.1 (0.1)	8.9 / 9.5 (0.1)		7.3 / 10.9 (2.4)
2b			10.9 / 11.6 (0.1)		
3a	14.7 / 13.4 (2.5)	14.9 / 13.3 (0.1)	14.5 / 15.0 (0.2)	15.5 / 8.1 (1.6)	13.9 / 12.6 (2.6)
3b		16.3 / 14.4 (0.1)	16.9 / 17.0 (0.2)	17.5 / 11.0 (1.9)	
4a	29.0 / 26.4 (3.6)	34.4 / 30.2 (0.3)	37.9 / 37.0 (0.4)		
4b	32.2 / 29.3 (3.8)				
5	57.5 / 33.6 (4.0)	57.2 / 48.3 (0.5)			
6a	77.2 / 51.4 (5.0)	76.6 / 63.0 (0.6)	71.0 / 68.7 (0.7)		
6b			88.7 / 84.7 (0.8)		
7a		179.4 / 162.0 (1.6)	149.9 / 144.4 (1.4)	166.0 / 37.5 (3.5)	
7b			185.4 / 183.3 (1.8)		
8a	322.4 / 192.5 (9.6)	338.5 / 304.9 (3.0)	378.8 / 370.6 (3.7)	306.3 / 53.8 (4.1)	320.0 / 114.7 (7.9)
8b				330.5 / 55.6 (4.2)	
10	870.5 / 689.8 (18.2)	806.0 / 689.0 (6.9)	838.2 / 808.8 (8.1)	838.2 / 92.1 (5.4)	806.0 / 203.1 (10.6)
11	1660.4 / 988.8 (21.8)	1620.1 / 1369.5 (13.7)	1636.2 / 1515.9 (15.2)	1652.3 / 130.9 (6.5)	
12a	3441.6 / 1694.4 (28.5)	3312.7 / 2818.4 (28.2)	3312.7 / 3149.5 (31.5)	3401.3 / 192.0 (7.8)	3248.2 / 457.2 (15.9)
12b		3385.2 / 2839.9 (28.4)		3433.6 / 203.8 (8.1)	3353.0 / 466.4 (16.0)
13a	6085.3 / 2286.7 (33.1)	6351.3 / 5316.3 (53.2)	6448.0 / 6183.1 (61.8)	6415.0 / 284.1 (9.5)	6286.8 / 625.6 (18.5)
13b	6464.1 / 2508.5 (34.7)			6464.1 / 294.9 (9.7)	6327.1 / 639.7 (18.8)

Table 8 – Coefficients derived from the linear region of the LUPIN, H-filled and Ar-filled chambers, expressed for each position in nSv per proton on dump, with the related uncertainties.

Position 1	Position 2	Position 3	Position 4	Position 5
$(8.71 \pm 0.44)\cdot10^{-10}$	$(5.37 \pm 0.27)\cdot10^{-10}$	$(5.13 \pm 0.26)\cdot10^{-10}$	$(6.90 \pm 0.35)\cdot10^{-10}$	$(8.06 \pm 0.40)\cdot10^{-10}$

4. Discussion

4.1. Analysis of the results

The detector responses in position 1 are shown as a function of the expected H*(10) in Figures 18-22. The plots of the responses in the other positions, very similar to those obtained in position 1, are reported for completeness in the Appendix. The line fitting the experimental data points is compared with a straight line that represents the bisector of the first quadrant, i.e. the ideal linear response. The equation used to fit the data was chosen only as a visual guide and is a power polynomial of the form $y = A\cdot x^B$.

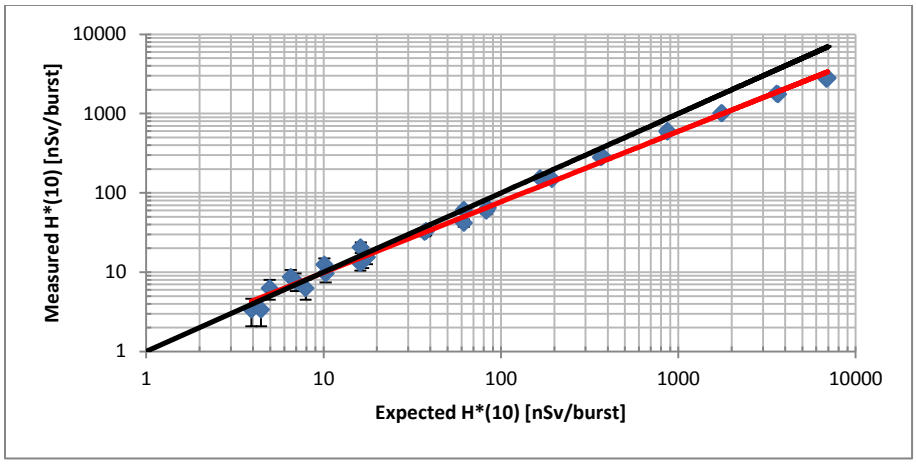

Figure 18 – Response of the LUPIN in position 1. The straight line is the bisector of the first quadrant, representing the ideal linear behaviour.

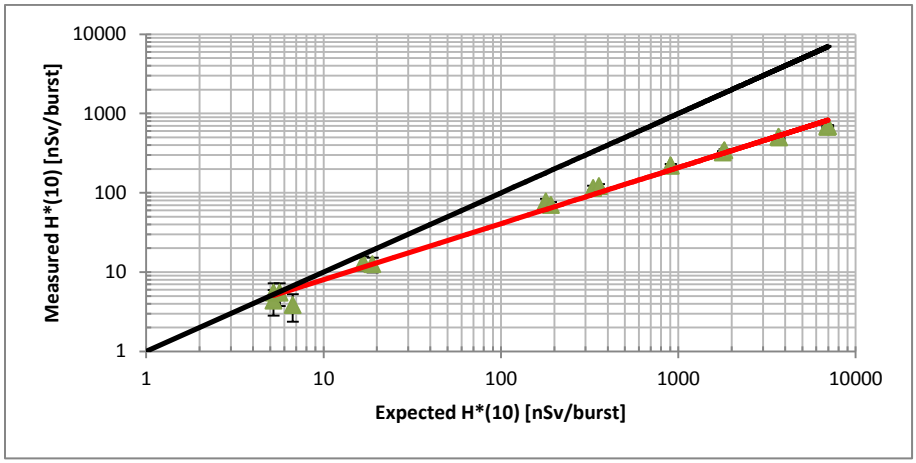

Figure 19 – Response of the BIOREM in position 1. The straight line is the bisector of the first quadrant, representing the ideal linear behaviour.

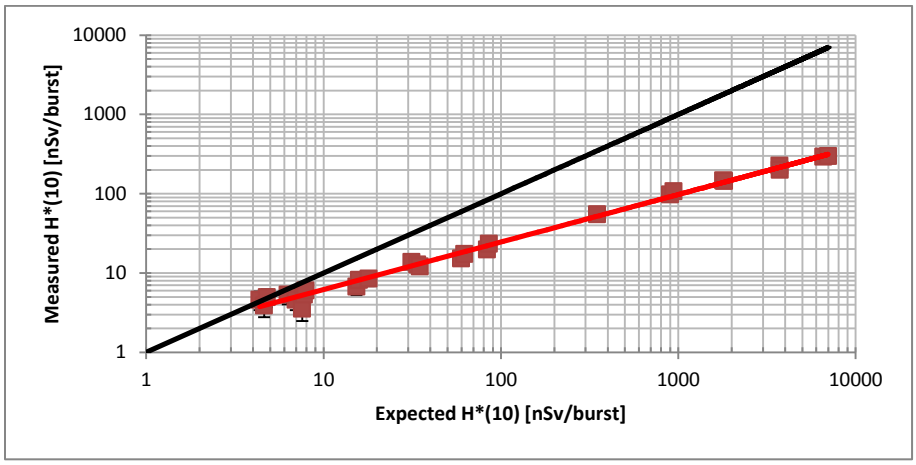

Figure 20 – Response of the Wendi-2 in position 1. The straight line is the bisector of the first quadrant, representing the ideal linear behaviour.

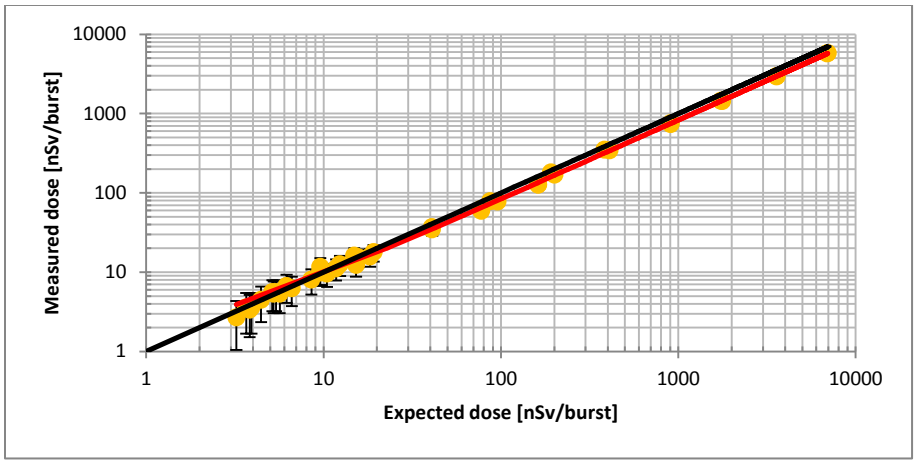

Figure 21 – Response of the Hydrogen-filled chamber in position 1. The straight line is the bisector of the first quadrant, representing the ideal linear behaviour.

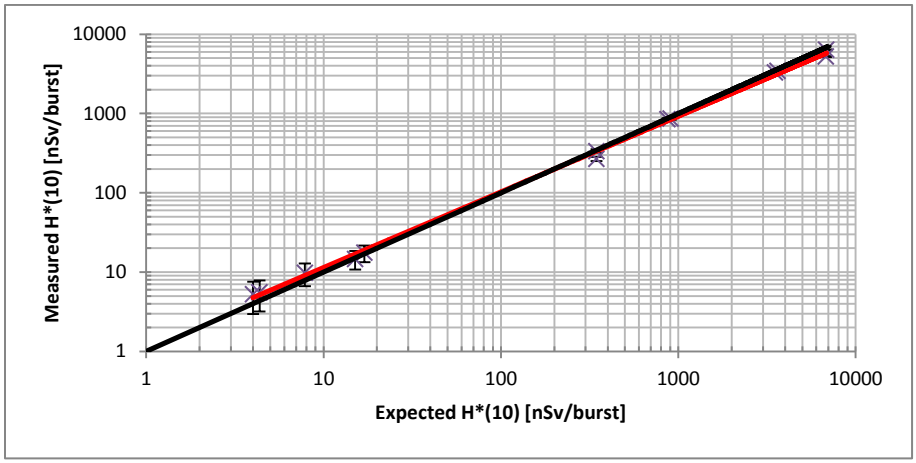

Figure 22 – Response of the Argon-filled chamber in position 1. The straight line is the bisector of the first quadrant, representing the ideal linear behaviour.

The response function is linear essentially over the entire H*(10) range for the Ar and H-filled chambers, with a slight underestimation only for values of expected H*(10) per burst higher than 1 µSv. For the other detectors the response is linear for low values of expected H*(10) and starts to saturate at higher intensities. The deviation from the ideal line is limited for the LUPIN, while it is of great importance for the BIOREM and the Wendi-2. Table 9 shows the ratios between the measured and the expected H*(10) averaged over all the positions for different values of expected H*(10) per burst. The ratios are not shown for values lower than 100 nSv/burst since the statistical uncertainties are too high to obtain a univocal value.

	Expected H*(10) per burst					
Detector	100 nSv	200 nSv	500 nSv	1 µSv	2 µSv	5 µSv
LUPIN	0.76	0.75	0.73	0.68	0.57	0.45
BIOREM	0.51	0.36	0.26	0.22	0.16	0.12
Wendi-2	0.25	0.20	0.13	0.10	0.07	0.05
H chamber	0.90	0.89	0.89	0.87	0.86	0.85
Ar chamber	1.00	0.98	0.97	0.97	0.97	0.96

Table 9 – Ratios measured/expected H*(10) per burst for different beam intensities.

The underestimation of the expected H*(10) is lower than 5% for the Ar-filled chamber and 15% for the H-filled chamber over the entire intensity range. The underestimation of the LUPIN is acceptable (< 30%) for expected

H*(10) up to 1 µSv/burst, while for the BIOREM and the Wendi-2 it is already very important for 100 nSv/burst (underestimation of a factor of 2 for the BIOREM, or a factor of 4 for the Wendi-2). At higher values of expected H*(10) the underestimation becomes of almost one order of magnitude for the BIOREM and the Wendi-2 that cannot therefore be considered reliable anymore, whereas for the LUPIN it is limited to a factor of 2.

The underestimation of the H*(10) is due to both electronics and physical reasons. The former comes from the fact that the instruments working in pulse mode (like the BIOREM and the Wendi-2) are affected by dead time losses, that can become rather severe when high counting rates are encountered, which is the case when detecting PNF. Dead time corrections can be applied by internal algorithms to try to compensate for the losses, but these algorithms operate properly in steady-state radiation fields, whereas their reliability is low when dealing with pulsed fields of unknown time structure and H*(10) in the burst. To derive the dead time for each detector, which is not known *a priori* and is dependent on unknown limiting properties of the counting system, the "two-source method" [24] was applied to the acquired data. The method is based on observing the counting rate from two sources individually and in combination. The method was applied by taking three different values of expected and measured counting rates, i.e. EXP_1, EXP_2, EXP_{12} and $MEAS_1$, $MEAS_2$, $MEAS_{12}$, where $EXP_{12} = EXP_1 + EXP_2$, and by evaluating them individually and in combination. The dead time could be calculated from the discrepancy between the measured rate $MEAS_{12}$ and the sum of $MEAS_1 + MEAS_2$. The obtained values are: (1.02 ± 0.10) µs for the BIOREM (very close to the TTL pulse width declared by the manufacturer, 1.2 µs [25]) and (1.74 ± 0.17) µs for the Wendi-2. For the LUPIN and the ionization chambers the calculation of the dead time would not have any physical meaning: in fact the LUPIN is not operating in pulse mode and the nature of the output pulses of the ionization chambers depends only on the characteristics of the digitizing circuit. It is clear from the derived values that the dead time losses are high for the BIOREM and the Wendi-2, whereas they are much lower for the two ionization chambers. This confirms the different level of underestimation noticed from the detector results.

The first physical reason explaining the detector underestimation regards proportional counters that use the integration of the total electric charge as a measure of the amount of the neutron signal, which is the case of the LUPIN. The underestimation comes from the diminution of the gas multiplication factor in the counter due to the shielding of the electric field, which is caused by accumulation of slow moving positive ions left behind by the multiplication process. This effect appears when neutrons interact with the detector during a time too short for the process of positive charge recollection [1].

A second physical reason explains the slight underestimation of the two ionization chambers. This is due to the incomplete ion collection caused by volume recombination, initial recombination and ion loss due to diffusion of ions to the collecting plates against the charge separating field. Among these processes only the losses due to volume recombination vary with the measured H*(10) [26]. This is taken into account by the manufacturer, which declares a possible maximum underestimation of the H*(10) of 15% when the ionization chambers are dealing with a charge per pulse in the order of tens of nC, i.e. what was seen for the higher intensities in this experiment [23].

Due to the special features of the LUPIN, the signal can be acquired and saved in a graphical form over a time that can be set by the user. It was then decided to extend up to 100 ms the acquisition window to cross-check the time distribution with the one predicted by FLUKA simulations. The signal acquired over a window of 100 ms is shown in Figure 23.

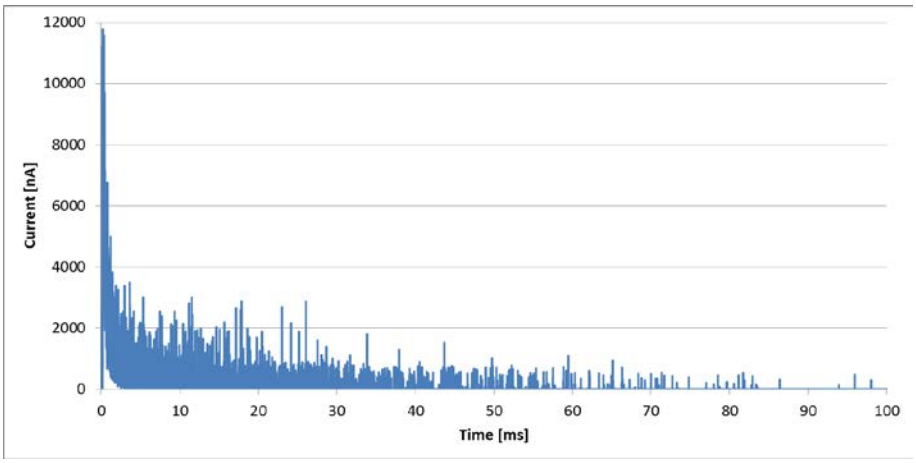

Figure 23 – Signal acquired with the LUPIN at beam setting 13 with an acquisition window of 100 ms.

If one compares the LUPIN signal with Figure 16 it can be seen that the time distribution as simulated by FLUKA is completely coherent with what was observed experimentally. After a first very intense part of the signal which is generated in the detector in the first 2 ms, the intensity progressively decreases, until the last neutrons are detected 100 ms later. When one compares the two figures, it should be taken into account that in Figure 16 t = 0 is the time when the beam impinges on the dump, while in Figure 23 t = 0 corresponds to the detection of the first neutron in the LUPIN. However, the time needed by the first neutron to reach the detector after the beam has hit the dump is negligible, i.e. about 2 µs according to the FLUKA simulations.

4.2. Fitting equation

In Figures 18-22 the fitting equation applied to the data is a power polynomial, used just to guide the eye. However, an attempt was made to find a fit that was more physically meaningful. Caresana et al. [2] formulated a method to fit the data obtained in a similar experiment at the Helmholtz Zentrum Berlin (HZB). The fitting equation expressed the transition between the linear and the saturation region via a parameter called D_{half}, typical of each detector, i.e. the value of reference H*(10) per burst at which the monitor underestimates by a factor of 2:

$$D_{meas} = \frac{D_{ref}}{1 + \frac{D_{ref}}{D_{half}}} \quad (1)$$

where D_{ref} is the expected H*(10) per burst and D_{meas} is the measured one. This fitting equation can be modified according to the specificities of this experiment, where the stray field conditions are different from the one observed at the HZB. In fact, as a consequence of the scattering that the neutrons encounter in the long tunnel, the stray field at the detector positions contains a significant delayed neutron component. Equation (1) can then be modified by adding an extra term:

$$D_{meas} = \frac{D_{ref}}{1 + \frac{D_{ref}}{D_{half}}} + k \cdot A \cdot D_{ref} \quad (2)$$

where k represents the percentage of the field (in terms of measured H*(10)) that is due to scattered neutrons and varies according to the experimental set-up: k = 0 in the HZB experiment, where the scattered component was negligible; k = 0.18 for these measurements, as calculated from the signals acquired via the LUPIN (see an example in Figure 24: the fraction of H*(10) integrated in the scattered component is 18% of the total).

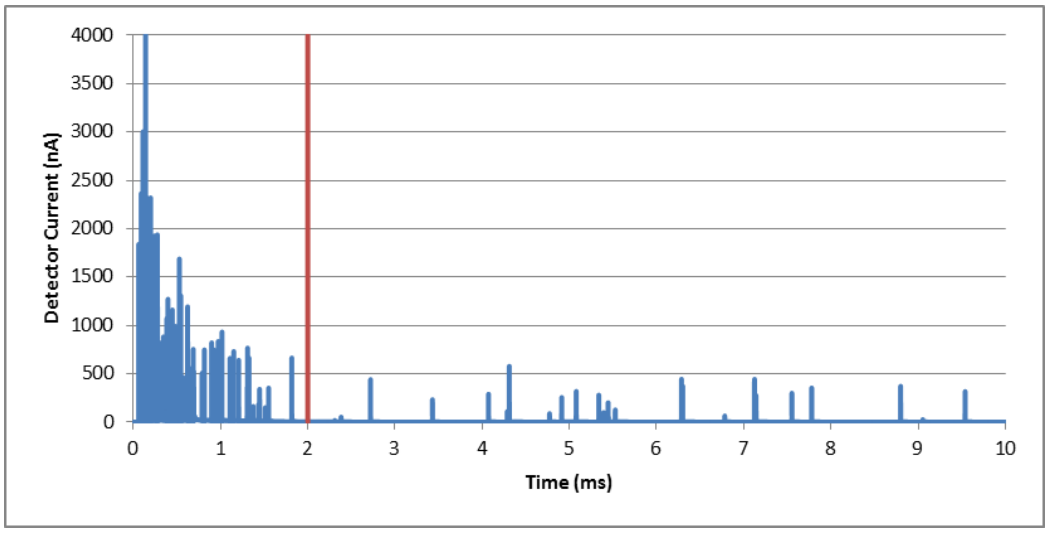

Figure 24 – Signal acquired with the LUPIN at beam setting 7. The red line splits the plot in two parts: the pulsed (left) and the scattered (right) component.

A is a parameter, function of D_{ref}, which describes the decreasing weight of the scattered part of the field as the H*(10) per burst increases. The expression of A used to fit the data of this experiment, for all the detectors in the five positions, is

$$A = 1 - 7 \cdot 10^{-5} \cdot D_{ref}. \quad (3)$$

However, the determination of the expression to be used for the parameter A is still under study and will require further investigations. The values of D_{half} used for the fitting were the same as the ones found in the HZB experiment [2] since they are dependent on the type of detector used and not on the field characteristics. Figure 25 shows the difference between the fitting equations (1) and (2) applied to a set of Biorem data.

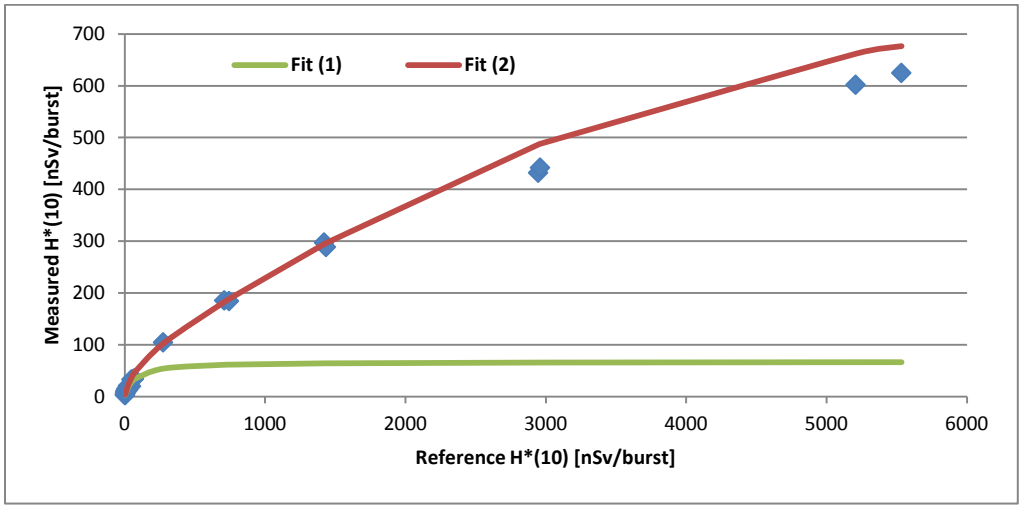

Figure 25 – Application of the fitting equation (1) (green line) and (2) (red line) on the data (blue points) acquired with the Biorem in position 4.

5. Conclusions

The work described in this paper allowed the study of the linearity of the response to PNF of five neutron detectors up to extreme stray field intensities. The special characteristics of the HiRadMat facility allowed the detectors to be tested in the stray field generated by a proton beam with tunable intensity impinging on the dump.

The stray field was only due to neutrons and this allowed focusing the attention on the analysis of the response, neglecting the problems related to the photon rejection. The primary beam intensity, the stray field intensity and therefore the expected H*(10) per burst could be varied over more than three orders of magnitude. Moreover, the presence of a significant delayed neutron component enabled the detectors to be tested in a pulsed stray field in which a slow contribution is also observed, i.e. in a radiation environment similar to that found in operational conditions.

According to the performance of the detectors, several conclusions can be drawn:

- the gas-filled (Hydrogen or Argon) ionization chambers used in the RAMSES monitoring system at CERN show a quasi-linear response, very close to the ideal behaviour, up to extreme values of H*(10) per burst that could be obtained in the experiment;
- the Wendi-2 and the BIOREM responses are characterized by a strong deviation from the linearity, especially noticeable in the Wendi-2, when the expected H*(10) per burst is higher than a few ten of nSv;
- the LUPIN response shows a slight deviation from the ideal curve for expected values of H*(10) higher than 100 nSv. The deviation becomes rather strong for the extreme beam intensities tested, but this device is nonetheless a very good candidate as both a portable and installed monitor at particle accelerator facilities where a strongly pulsed neutron component is present.

Expression (2) proved able to correctly fit the data obtained with the different detectors in the experiment. This formula is based on physical reasons and its use can potentially be extended to all the cases in which a neutron detector is used in PNF. Moreover, it could be implemented for a generic detector in an internal algorithm to compensate for saturation losses. The formula is composed of two terms: the first describing the detector response as a pure dependence on the pulsed component of the field, the second related to the scattered part. It depends on three parameters: D_{half}, k and A. D_{half} depends only on the detector and the values used here were taken, when possible, from the values given in ref. [2]; k depends on the weight of the scattered component of the field; A describes the decreasing weight of the scattered part of the field as the value of H*(10) per burst increases.

The effectiveness of the fitting equation needs to be further verified, as it has been applied only to the data acquired in this experiment and, by imposing $k = 0$, to the data obtained in the HZB experiment [2]. Other systematic studies conducted to test the response of detectors in PNF do not seem to be present in the literature. Therefore further investigations are needed to confirm the general applicability of the method.

Acknowledgements

The authors wish to thank Ilias Efthymiopoulos for his overall support and for useful technical discussions, and Kurt Weiss and Dino De Paoli for their technical help during the installation and during the measurements. The authors are indebted to Frederic Loprete for his meticulous work in the construction of the aluminium support under a tight time schedule. The authors also wish to thank Doris Forkel-Wirth for her continuous support in this experimental activity. This experiment was partially funded by EuCARD Transnational Access HiRadMat@SPS. This research project has been also supported by a Marie Curie Early Initial Training Network Fellowship of the European Community's Seventh Framework Programme under contract number PITN-GA-2011-289198-ARDENT.

REFERENCES

[1] I. Rios, J. Gonzalez, R.E. Mayer, Total fluence influence on the detected magnitude of neutron burst using proportional detectors, Rad. Meas., in press, accepted manuscript.

[2] M. Caresana, A. Denker, A. Esposito, M. Ferrarini, N. Golnik, E. Hohmann, A. Leuschner, M. Luszik-Bhadra, G. Manessi, S. Mayer, K. Ott, J. Röhrich, M. Silari, F. Trompier, M. Wielunski, Intercomparison of radiation protection instrumentation in a pulsed neutron field, Nucl. Instrum. Meth. A, in press.

[3] I. Efthymiopoulos, C. Hessler, H. Gaillard, D. Grenier, M. Meddahi, P. Trilhe, A. Pardons, C. Theis, N. Charitonidis, S. Evrard, H. Vincke, M. Lazzaroni, HiRadMat: A new irradiation facility for material testing at CERN, Proceedings of IPAC 2011, San Sebastien, Spain, 4-9 September 2011, TUPS058.

[4] M. Caresana, M. Ferrarini, G.P. Manessi, M. Silari, V. Varoli, LUPIN, a new instrument for pulsed neutron fields, Nucl. Instrum. Meth. A 712 (2013) 15-26.

[5] M. Caresana, M. Ferrarini, G. P. Manessi, M. Silari, V. Varoli, A neutron detector for pulsed mixed fields: preliminary measurements, Proceedings of the 12th International Conference on Radiation Shielding, Nara, Japan, 2-7 September 2012, published in Progress in Nuclear Science and Technology, in press.

[6] M. Ferrarini, V. Varoli, A. Favalli, M. Caresana, B. Pedersen, A wide dynamic range BF_3 neutron monitor with front-end electronics based on a logarithmic amplifier, Nucl. Instrum. Meth. A 613 (2010) 272-276.

[7] G. Segura Millan, D. Perrin, L. Scibile, RAMSES: the LHC radiation monitoring system for the environment and safety, Proceedings of the 10th International Conference on Accelerator & Large Experimental Physics Control Systems, Geneva, Switzerland, 10-14 October 2005, TH3B.1-3O (2006).

[8] P. Astier, D. Autiero, A. Baldisseri, M. Baldo-Ceolin, M. Banner, G. Bassompierre, K. Benslama, M. Besson, I. Bird, B. Blumenfeld et al., Prediction of neutrino fluxes in the NOMAD experiment, Nucl. Instrum. Meth. A 515 (2003) 800-828.

[9] D. Grenier, A. Pardons, TED-type beam dump, CERN Technical Note, EDMS No. 1145913.

[10] D.B. Pelowitz, MNCPXTM user's manual, Version 2.6.0, Los Alamos National Laboratory Report LA-CP-078-1473 (2007).

[11] D. Dumitrescu, A. Chirosca, Neutron field correction coefficients for active and passive dosimeters in Cernavoda NPP, Optoelectron. Adv. Mat. 5 (2011) 690-695.

[12] L. Jägerhofer, E. Feldbaumer, C. Theis, S. Roesler, H. Vincke, A new method to calculate the response of the Wendi-2 rem counter using the FLUKA Monte Carlo code, Nucl. Instrum. Meth. A 691 (2012), 81-85.

[13] R.H. Olsher, H.H. Hsu, A. Beverding, J.H. Kleck, W.H. Casson, D.G. Vasilik, R.T. Devine, Wendi: an improved neutron rem meter, Health Phys. 79 (2000) 170-181.

[14] R.H. Olsher, T.D. McLean, High-energy response of the PRESCILA and Wendi-II neutron rem meters, Rad. Prot. Dosim. 130 (2008) 510-513.

[15] C. Theis, The radiation environment in underground workplaces of the LHC, PhD thesis, Graz University of Technology, 2007, chapter 2.

[16] C. Theis, M. Rettig, S. Roesler, H. Vincke, Simulation and experimental verification of the response functions of Centronic high-pressure ionisation chambers, CERN-SC-2004-23-RP-TN (2004).

[17] N. Charitonidis, G.P. Manessi, M. Silari, Test run for the HRMT-15 (RPNIST) experiment, CERN Technical Note CERN-DGS-2012-092-RP-TN (2012).

[18] N. Charitonidis, E. Harrouch, Round detector support for HRM-15 (RPINST) experiment, CERN Technical Note, EDMS No. 1249864.

[19] G. Battistoni, S. Muraro, P.R. Sala, F. Cerutti, A. Ferrari, S. Roesler, A. Fasso, J. Ranft, The FLUKA code: description and benchmarking in: Proceedings of the Hadronic Shower Simulation Workshop, Batavia, USA, 6-8 September 2006, AIP Conference Proceeding 896 (2007) 31-49.

[20] A. Fasso, A. Ferrari, J. Ranft, P.R. Sala, FLUKA: a multi-particle transport code, CERN Technical Note, CERN-2005-10, INFN/TC_05/11, SLAC-R-773, 2005.

[21] N. Charitonidis, I. Efthymiopoulos, C. Theis, H. Vincke, Prompt, activation and background radiation studies for the HiRadMat facility of CERN/SPS, CERN Technical Note, EDMS No. 1144976.

[22] V. Vlachoudis, FLAIR: a powerful but user friendly graphical interface for FLUKA, Proceedings of the International conference on mathematics, computational methods and reactor physics, Saratoga, USA, 3-7 May 2009.

[23] M. Latu, Radiation monitoring system for the environment and safety, CERN Technical Note (in French), EDMS No. 770397.

[24] G.F. Knoll, Radiation detection and measurement, John Wiley & Sons Inc, 4th edition (2010), pp. 124-126.

[25] Thermo Scientific FHT 725 / FHT 752 H user's manual, Version 28.02.08.

[26] J. Bohm, Saturation corrections for plane-parallel ionization chambers, Phys. Med. Biol. 21 (1976) 754-759.

Appendix - Figure A1

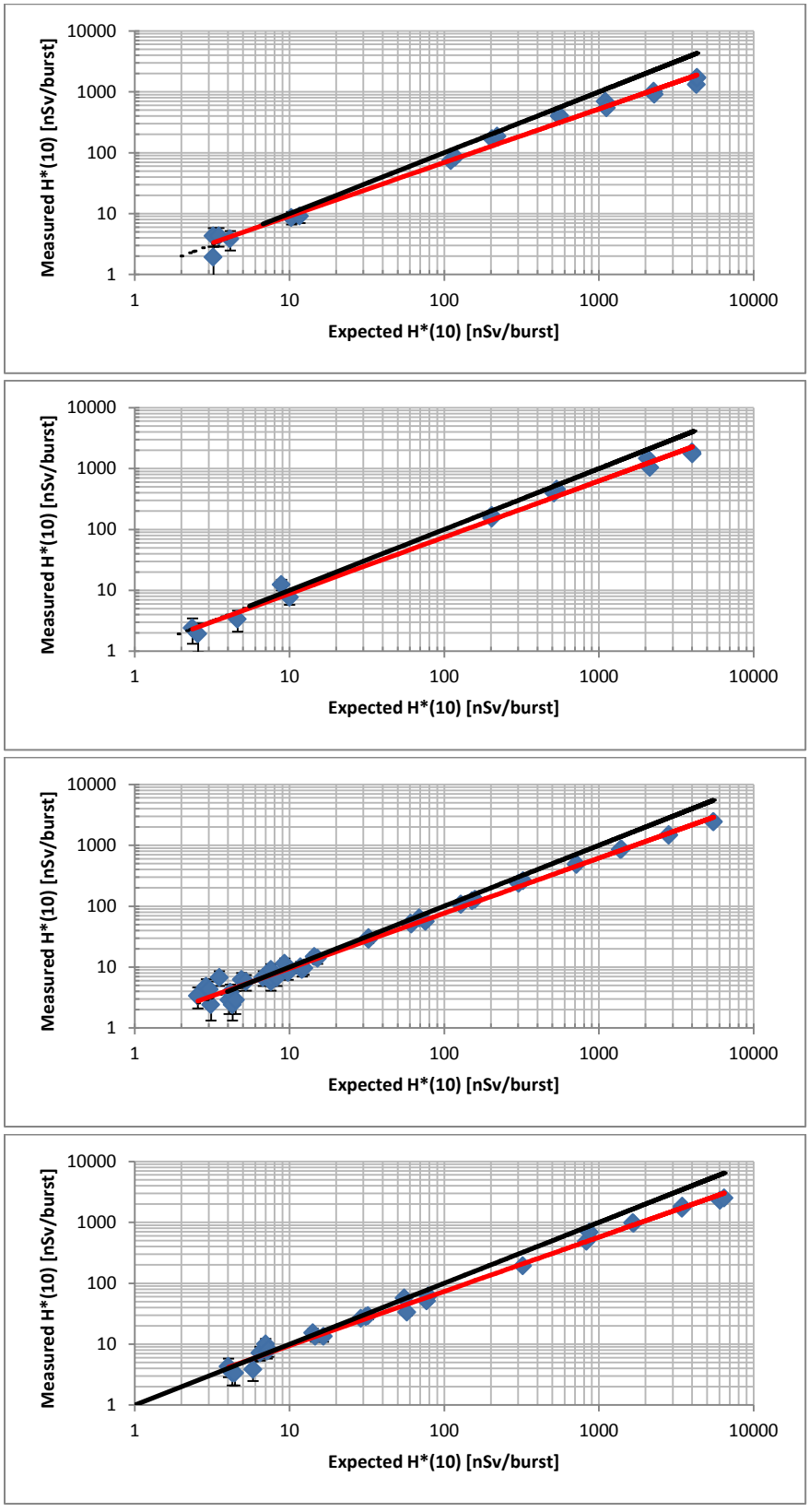

Figure A1 - Response of the LUPIN in positions 2-5 (top to bottom).

Figure A2

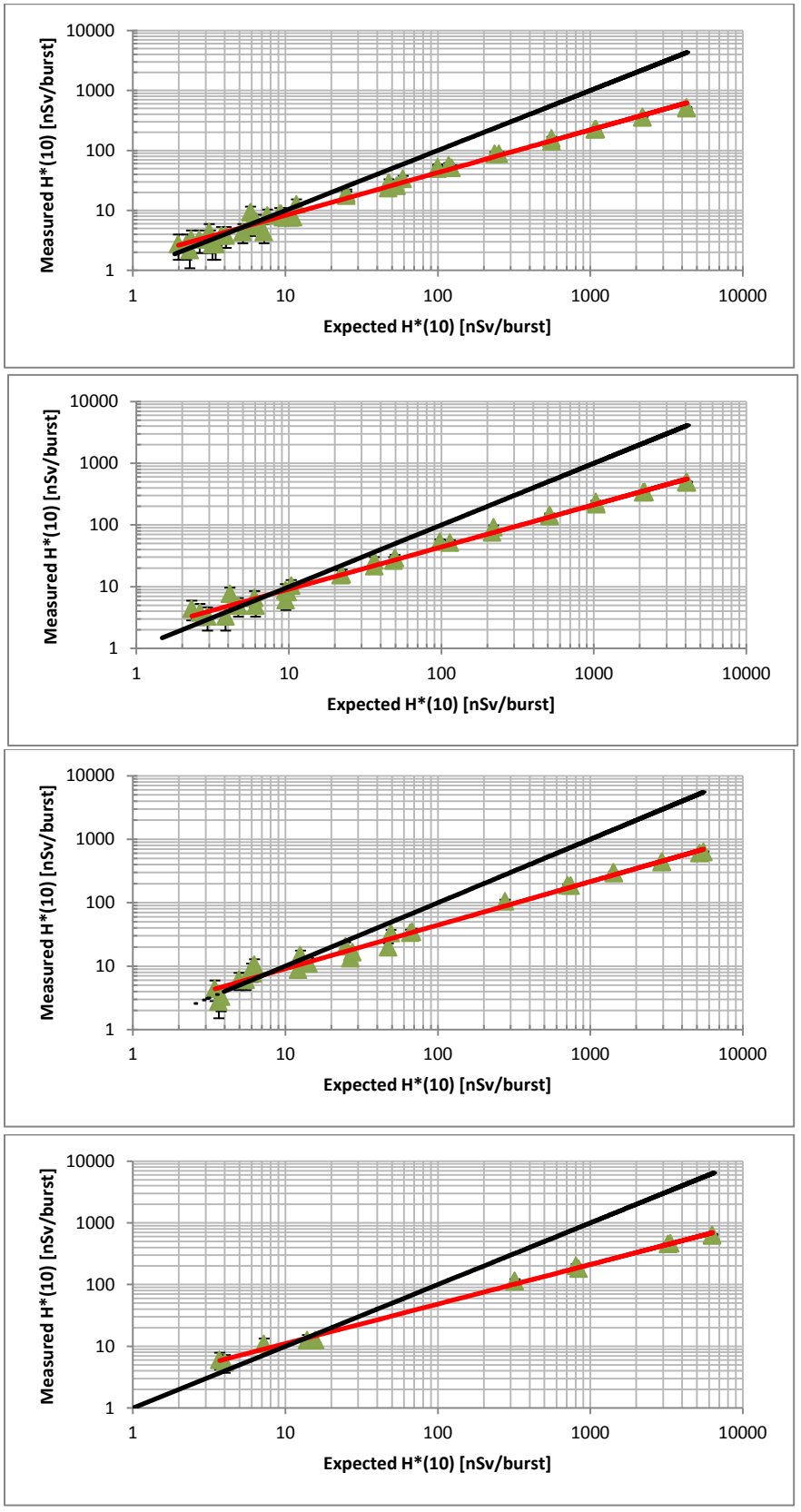

Figure A2 – Response of the BIOREM in positions 2-5 (top to bottom).

Figure A3

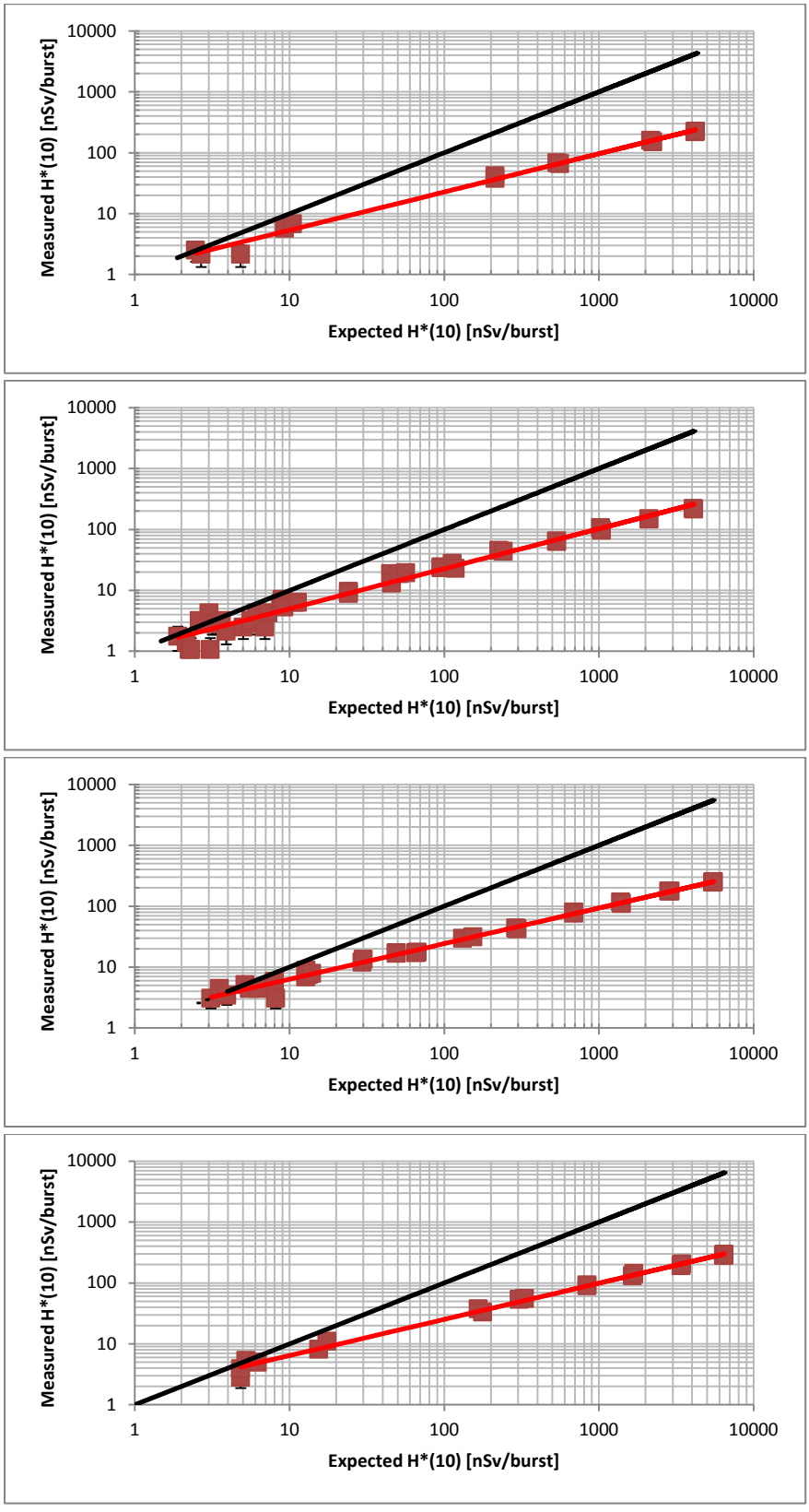

Figure A3 – Response of the Wendi-2 in positions 2-5 (top to bottom).

Figure A4

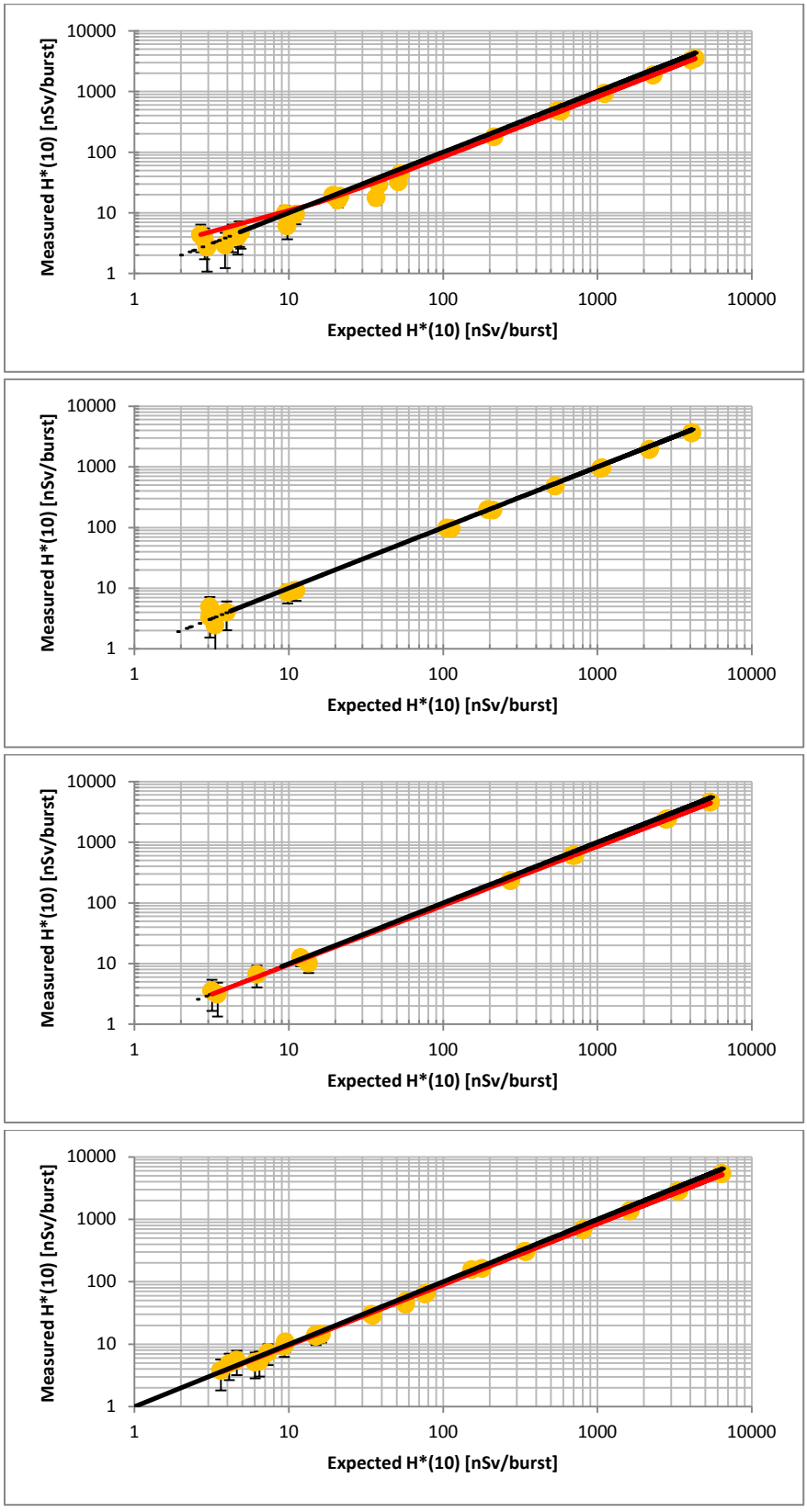

Fig A4 - Response of the Hydrogen-filled chamber in positions 2-5 (top to bottom).

Figure A5

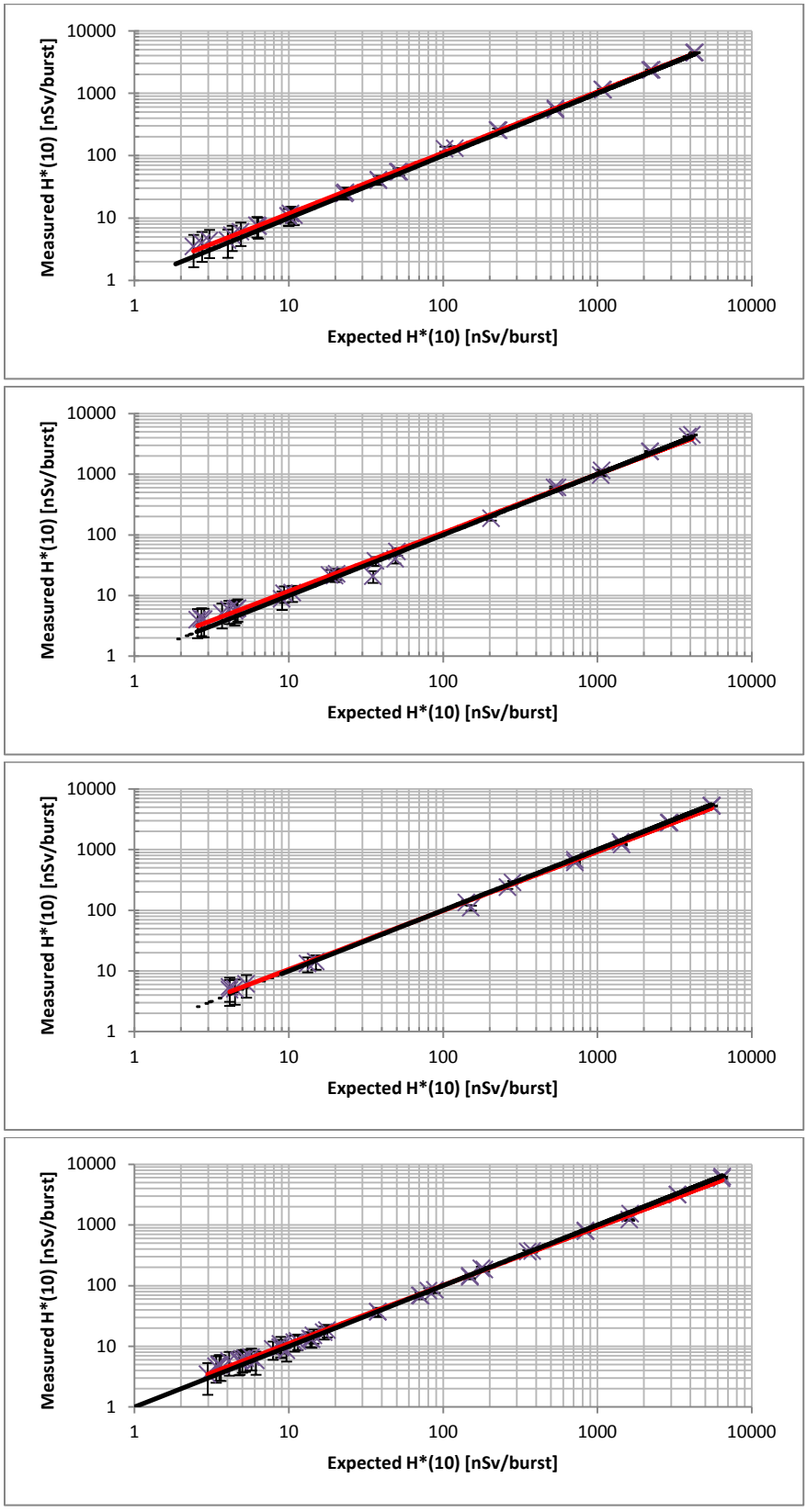

Figure A5 – Response of the Argon-filled chamber in positions 2-5 (top to bottom).